Hao *et al. Cell Communication and Signaling* (2025) 23:218
https://doi.org/10.1186/s12964-025-02209-9

Cell Communication
and Signaling

RESEARCH **Open Access**

# Strong protection by bazedoxifene against chemically-induced ferroptotic neuronal death *in vitro* and *in vivo*

Xiangyu Hao[1], Yifan Wang[1], Ming-Jie Hou[1], Yong Xiao Yang[1], Lixi Liao[1], Tongxiang Chen[1], Pan Wang[1], Xiaojun Chen[2] and Bao Ting Zhu[1,3*]

## Abstract

Ferroptosis, a form of regulated cell death associated with glutathione depletion and excess lipid peroxidation, can be induced in cultured cells by chemicals (*e.g.*, erastin and RSL3). It has been shown that protein disulfide isomerase (PDI) is a mediator of chemically-induced ferroptosis and also a crucial target for ferroptosis protection. The present study reports that bazedoxifene (BAZ), a selective estrogen receptor modulator, is an inhibitor of PDI and can strongly rescue neuronal cells from chemically-induced oxidative ferroptosis. We find that BAZ can directly bind to PDI and inhibit its catalytic activity. Computational modeling analysis reveals that BAZ forms a hydrogen bond with PDI's His256 residue. Inhibition of PDI by BAZ markedly reduces iNOS and nNOS dimerization (*i.e.*, catalytic activation) and NO accumulation, and these effects of BAZ are associated with reductions in cellular ROS and lipid-ROS and protection against chemically-induced ferroptosis. In addition, the direct antioxidant activity of BAZ may also partially contribute to its protection against chemically-induced ferroptosis. *In vivo* animal experiments show that mice treated with BAZ are strongly protected against kainic acid-induced oxidative hippocampal neuronal injury and memory deficits. Together, these results reveal that BAZ is a potent inhibitor of PDI and can strongly protect against chemically-induced ferroptosis in hippocampal neurons both *in vitro* and *in vivo*. This work provides evidence for an estrogen receptor-independent, PDI-mediated novel mechanism of neuroprotection by BAZ.

**Keywords** Ferroptosis, Protein disulfide isomerase, Selective estrogen receptor modulator, Bazedoxifene, Nitric oxide synthase, Nitric oxide, Reactive oxygen species

## Significance statement

Ferroptosis is an iron- and lipid peroxidation-dependent form of regulated cell death. Recent evidence has shown that protein disulfide isomerase (PDI) is an important mediator of chemically-induced ferroptosis and also a new target for ferroptosis protection. We find that bazedoxifene is an inhibitor of PDI, which can strongly protect against chemically-induced ferroptotic neuronal death *in vitro* and *in vivo*. Additionally, the molecular mechanism of PDI–bazedoxifene binding interaction is defined. This work provides evidence for an estrogen receptor-independent, PDI-mediated novel mechanism of neuroprotection by bazedoxifene.

---

*Correspondence:
Bao Ting Zhu
BTZhu@CUHK.edu.cn
[1] Shenzhen Key Laboratory of Steroid Drug Discovery and Development, School of Medicine, The Chinese University of Hong Kong, 2001 Longxiang Road, Longgang District, Shenzhen 518172, China
[2] Department of Gynecology, Obstetrics and Gynecology Hospital, Fudan University, Shanghai, China
[3] Shenzhen Bay Laboratory, Shenzhen 518055, China

## Introduction

Ferroptosis is a form of regulated cell death closely associated with glutathione (GSH) depletion and/or glutathione peroxidase 4 (GPX4) inhibition, both of which can lead to accumulation of lipid reactive oxygen species (ROS), and ultimately oxidative cell death [1–7]. There is increasing evidence showing that ferroptosis is an important contributor in many forms of ischemic organ injuries (*e.g.*, ischemic heart disease and ischemic kidney and brain injuries) [8–10] and in chemically-induced organ damage (*e.g.*, acetaminophen-induced liver and kidney damage) [11, 12]. Studies have shown that pharmacological inhibition of ferroptosis can significantly reduce ischemia/reperfusion-associated organ injury [13, 14] and chemically-induced liver damage [11, 15, 16]. In addition, mounting evidence also links ferroptosis to various neurodegenerative conditions, such as hemorrhagic stroke, Alzheimer's disease, Parkinson's disease and Huntington's disease [17–21]. These neurodegenerative conditions often exhibit ferroptosis-related characteristics, such as elevated lipid peroxidation, mitochondrial dysfunction, and reduced level of GPX4 [22–25]. A number of ferroptosis inhibitors have been shown to exhibit a protective effect in animal models of neurodegeneration and injury [22, 24, 26].

Protein disulfide isomerase (PDI or PDIA1) is an ubiquitous dithiol/disulfide oxidoreductase of the thioredoxin superfamily [27–29]. PDI is mostly found in the endoplasmic reticulum of mammalian cells, although it is also present in the nucleus, cytosol, mitochondria, plasma membrane and extracellular space [29]. PDI is involved in protein processing by catalyzing the interconversion (isomerization) between free thiols and disulfide bounds in proteins [30]. In recent years, we have shown that PDI plays an important role in mediating the oxidative cytotoxicity in HT22 mouse hippocampal neuronal cells challenged with inducers of oxytosis/ferroptosis, including glutamate [31], erastin [32], RSL3 [33] and sulfasalazine [34] Mechanistically, we have shown that glutamate- or erastin-induced GSH depletion can lead to oxidation of PDI's thiol groups, which results in PDI catalytic activation for NOS dimerization, accumulation of cellular NO, ROS and lipid-ROS, and ultimately, oxidative cell death (oxytosis/ferroptosis) [31, 32]. In comparison, RSL3 induces ferroptosis by jointly inhibiting GPX4 and thioredoxin reductase 1 (TrxR1) [33, 35]. TrXR1 inhibition by RSL3 facilitates PDI activation (*i.e.*, oxidation of the free thiol groups in PDI's catalytic sites), which is followed by NOS dimerization and accumulation of cellular NO and ROS/lipid-ROS and induction of ferroptosis [33]. We have shown that pharmacological inhibition of PDI's catalytic function or genetic manipulation of PDI expression each can effectively abrogate the induction of oxytosis/ferroptosis in HT22 cells following exposure to glutamate [31], erastin [32], RSL3 [33] and sulfasalazine [34]. Together, these studies reveal that PDI is a key mediator of chemically-induced oxytosis/ferroptosis, and also highlight PDI as a target for protection against oxidative neuronal death.

Bazedoxifene (BAZ), a synthetic selective ER modulator (SERM, structure shown in Fig. 1A), is approved for use in the U.S. for treatment of osteoporosis in postmenopausal women [36, 37]. In addition, BAZ is also being tested for its direct anticancer activity in humans (*e.g.*, breast cancer) [38], or as an anticancer adjuvant to enhance the chemotherapeutic efficacy of other anticancer drugs [39–42]. Interestingly, there have been reports in recent years on the protective effects of certain SERMs, including raloxifene and BAZ, in neurons and glial cells [43–45]. An earlier study has been suggested that the protective actions of SERMs may involve activation of the estrogen receptors and/or the G protein-coupled receptor for estrogens (GRP30), through increased expression of antioxidants and activation of kinase-mediated survival signaling pathways [46]. Recently, we have showed that raloxifene indeed has a strong neuroprotective effect against chemically-induced ferroptosis, and this effect is attributed to its ability to inhibit PDI-mediated NOS dimerization [47]. However, it is not known whether BAZ shares this neuroprotective action.

(See figure on next page.)

**Fig. 1** Protective effect of BAZ against erastin-induced ferroptosis in HT22 cells. **A.** Chemical structure of bazedoxifene (BAZ). **B**, **C**. Cytotoxicity of erastin alone (**B**) and its protection by BAZ (**C**) after 24-h treatment with erastin ± BAZ at indicated concentrations (MTT assay, *n* = 5). **D**. Calcein-AM/PI double staining of live and dead cells following 8-h treatment with 0.8 μM erastin ± 1 μM BAZ (fluorescence microscopy images, scale bar = 60 μm). **E**–**G**. mRNA levels of *GPX4* (**E**), *PTGS2* (**F**) and *ACSL4* (**G**). Cells were treated with 0.8 μM erastin ± 1 μM BAZ for 2 h (for detection of *PTGS2*) or 8 h (for detection of *GPX4* and *ACSL4*), and then their mRNA levels were determined by RT-qPCR (*n* = 3). **H**. Cellular levels of GPX4, COX2 and FACL4 proteins after 8-h treatment with 0.8 μM erastin ± 1 μM BAZ (Western blotting). **I**–**K**. Cellular levels of NO (**I**), ROS (**J**) and lipid-ROS (**K**) after 8-h treatment with 0.8 μM erastin ± 1 μM BAZ (analytical flow cytometry). The left panels of **I**, **J**, **K** are the histograms, and the right panels are respective quantitative intensity values (*n* = 3). **L**. Cellular levels of lipid-ROS after 8-h treatment with 0.8 μM erastin ± 1 μM BAZ. The cells were stained with BODIPY and Hoechst, and then subjected to confocal microscopy (scale bar = 10 μm). **M.** Levels of mitochondrial ROS after 8-h treatment with 0.8 μM erastin ± 1 μM BAZ. The cells were stained with MitoSOX, MitoTracker and Hoechst, and then subjected to confocal microscopy (scale bar = 10 μm). Quantitative data are presented as mean ± S.D. (* or $^{\#}$ $P < 0.05$; ** or $^{\#\#}$ $P < 0.01$)

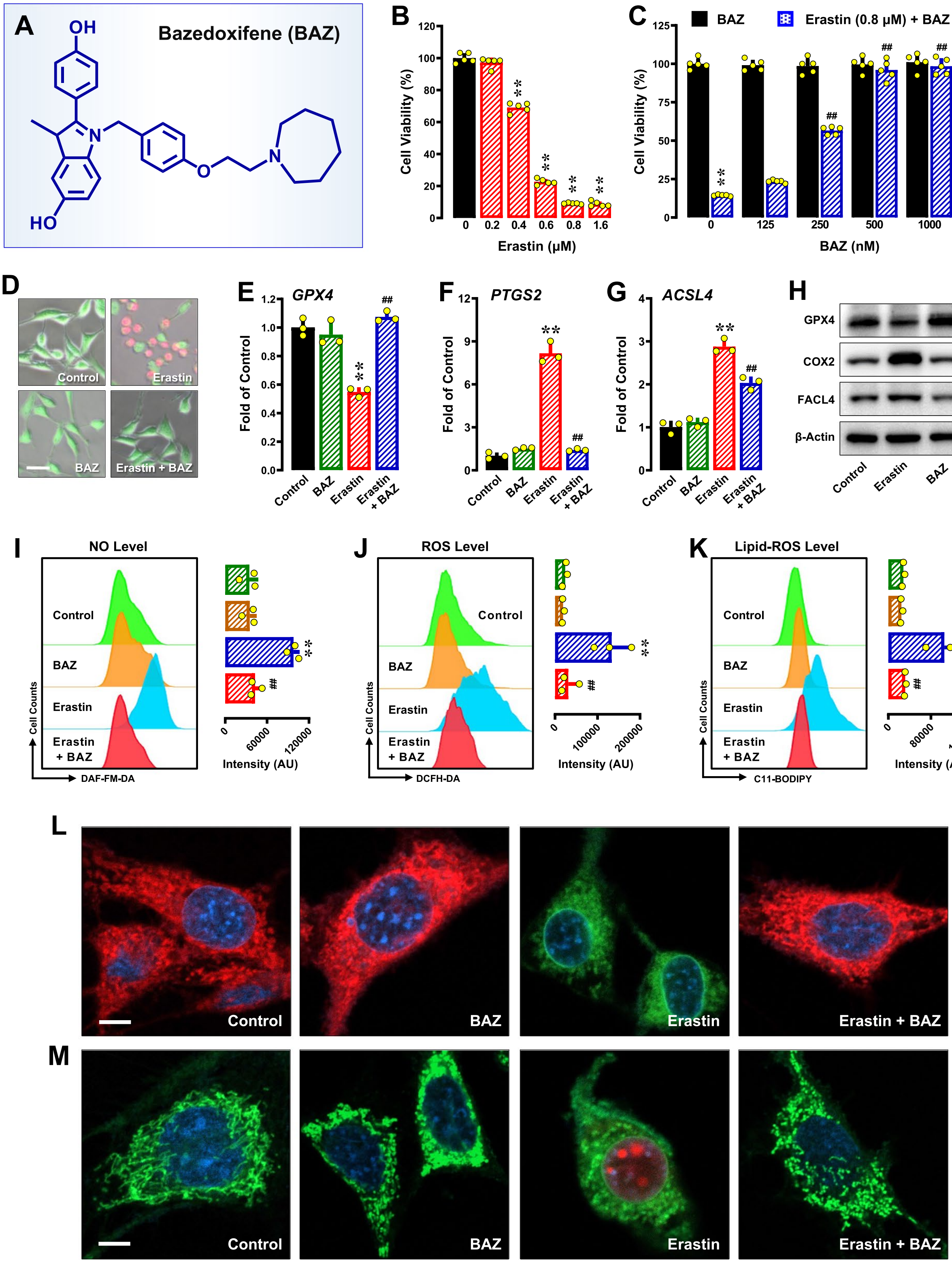

**Fig. 1** (See legend on previous page.)

The present study seeks to determine the neuroprotective effect of BAZ against chemically-induced ferroptotic neuronal death using both *in vitro* and *in vivo* models, with a focus on determining whether BAZ exerts its neuroprotection through altering PDI function and its downstream pathways. For *in-vitro* study, erastin and RSL3 were selected as inducers of oxidative ferroptosis in HT22 mouse hippocampal neurons. For the *in-vivo* study, kainic acid was used as an inducer of oxidative injury in mouse hippocampal neurons. Recently, it was reported that the brains of kainic acid-treated mice have reduced levels of GSH, which is coupled with increased levels of MDA, intracellular superoxide and lipid peroxides, increased PTGS2 and ACSL4 expression, and decreased GPX expression [48–53]. These changes indicate the induction of ferroptosis-related oxidative neuronal injury in kainic acid-injected brains. We find that BAZ can strongly rescue hippocampal neuronal cells from erastin/RSL3-induced ferroptosis *in vitro* and kainic acid-induced injury *in vivo*. Mechanistically, BAZ binds tightly to PDI and inhibits its catalytic activity, resulting in reduced NOS dimerization and NO accumulation, ultimately reduced ROS/lipid-ROS accumulation and ferroptotic neuronal death.

## Experimental procedures

### Chemicals

BAZ (#HY-A0031) and kainic acid (#HY-N2309) were obtained from MedChemExpress (Monmouth Junction, NJ, USA), and dissolved in pure dimethyl sulfoxide (DMSO) and saline, respectively, to prepare their stock solutions (at 10 mM). Erastin (#S7242) and methyl-(1S,3R)– 2-(2-chloroacetyl)– 1-(4-methoxycarbonylphenyl)– 1,3,4,9-tetrahydropyrido[3,4-b] indole- 3-carboxylate (RSL3, #S8155) were purchased from Selleck Chemicals (Houston, TX, USA), and their stock solutions (at 1 mM) were prepared in DMSO. 2',7'-Dichlorodihydrofluorescein diacetate (DCFH-DA, #S0033S) and 3-amino,4-aminomethyl- 2',7'-difluorescein diacetate (DAF-FM-DA, #S0019S) were purchased from Beyotime Biotechnology (Shanghai, China). MitoSOX (#M36008), MitoTracker green (#M7514), BODIPY-581/591-C11 (#D3861) and Hoechst (#H21486) were obtained from ThermoFisher (Waltham, MA, USA). O58 (#BB- 460652) was obtained from BestBio (Shanghai, China). Insulin (#I8830) was obtained from Solarbio (Beijing, China). Urea (#U5378), Ribonuclease A (RNase A, #R6513) and Cytidine 2′:3′-cyclic monophosphate monosodium salt (ccmp, #C9630) was obtained from Sigma-Aldrich (Waltham, MA, USA).

### Cell culture and cell viability assay

The HT22 mouse hippocampal neuronal cells, MDA-MB- 231 human breast cancer cells, H9 C2 rat myocardium cells and BRL- 3 A rat liver cells were obtained from the Cell Bank of Chinese Academy of Sciences (Shanghai, China), and were maintained in DMEM supplemented with 10% (*v*/*v*) fetal bovine serum (FBS, ThermoFisher, Waltham, MA, USA) and antibiotics (containing 100 U/mL penicillin and 100 μg/mL streptomycin; Sigma-Aldrich). Cells were cultured at 37℃ under 5% $CO_2$. Cell viability was determined by the MTT assay as described earlier [54]. Cells were authenticated by STR profiling and routinely tested for mycoplasma contamination.

### Staining of live and dead cells

Live and dead cells in culture were distinguished using the Calcein-AM and propidium iodide (PI) double staining method, according to the instructions of the manufacturer (Solarbio, Beijing, China). Briefly, after treatment of HT22 cells with selected chemicals, 1 μM Calcein-AM and 2.5 μM PI were added to the culture medium and the cells were cultured for an additional 30 min at 37 °C in the dark. Images of the cultured cells were then taken using a Nikon Eclipse Ti-U inverted microscope (Nikon, Tokyo, Japan).

### Quantitative real-time polymerase chain reaction (RT-qPCR)

Total RNAs in cells were sequentially extracted with the TRIzol reagent (#15596018; Invitrogen, Waltham, Massachusetts, USA) and chloroform, precipitated with isopropyl alcohol, and then washed with 75% ethanol to dissolve RNAs in the RNase-free sterile water. The cDNAs were synthesized with the Hifair III 1st Strand cDNA Synthesis Kit (#R312, Vazyme Biotech, Nanjing, China). Subsequently, RT-qPCR was performed using PerfectStart Green qPCR SuperMix (#AQ602, TransGen Biotech, Beijing, China) on an Applied Biosystems Quant Studio 3 (ThermoFisher, Waltham, MA, USA). Relative gene expression was calculated using the $2{-}\Delta\Delta C_t$ method, with GAPDH serving as an internal control. All primers (sequences are shown in Table 1) were synthesized by Sangon Biotech (Shanghai, China).

### Measurement of cellular NO and ROS by fluorescence microscopy

Cells were plated in 24-well places at a density of $5 \times 10^4$ per well and treated with drugs or chemicals for selected durations. For fluorescence staining, cells were first washed twice with HBSS and then incubated with DAF-FM-DA (5 μM, for cellular NO) and DCFH-DA (5 μM, for cellular ROS) in 200 μL DMEM (free of phenol red

**Table 1** Primer sequences used in the RT-qPCR analysis

| Target gene | Forward primer (5′→ 3′) | Reverse primer (5′→ 3′) |
|---|---|---|
| **GPX4 (mouse)** | GCCTGGATAAGTACAGGGGTT | CATGCAGATCGACTAGCTGAG |
| **PTSG2 (mouse)** | TTCAACACACTCTATCACTGGC | AGAAGCGTTTGCGGTACTCAT |
| **ACSL4 (mouse)** | CTCACCATTATATTGCTGCCTGT | TCTCTTTGCCATAGCGTTTTTCT |
| **GAPDH (mouse)** | AGGTCGGTGTGAACGGATTTG | TGTAGACCATGTAGTTGAGGTCA |

and serum) for 20 min at 37 °C. Following three washes with HBSS, fluorescence images were captured using an AXIO fluorescence microscope (Carl Zeiss Corporation, Germany).

### Measurement of cellular NO, ROS, lipid-ROS and peroxynitrite by flow cytometry

Cells were seeded in 6-well plates at a density of $15 \times 10^4$ cells/well 24 h before treatment with different drugs. Following drug treatment, cells were trypsinized, collected and suspended in phosphate-buffered saline (PBS). Cells were then centrifuged, and the resulting cell pellets were resuspended in DMEM (free of phenol red and serum) containing DAF-FM-DA (5 μM), DCFH-DA (5 μM), BODIPY- 581/591-C11 (5 μM) or O58 (1:2000 dilution of the original solution; for detection of peroxynitrite). After a 20-min incubation at 37 °C, the cells were washed three times with HBSS to remove any remaining fluorescent dyes. Levels of cellular NO, ROS, lipid-ROS and peroxynitrite were measured using flow cytometry (Beckman Coulter, Brea, CA, USA) and analyzed using the FlowJo software (FlowJo, LLC, Ashland, USA).

### Measurement of lipid-ROS and mitochondrial ROS by confocal microscopy

Cells were seeded at a density of $10 \times 10^4$ per well on coverslips placed inside the 12-well plates. Twenty-four h later, cells were treated with selected chemicals as indicated. Coverslips were then washed in HBSS and incubated in HBSS containing BODIPY- 581/591-C11 (5 μM, for lipid-ROS), MitoSOX (5 μM, for mitochondrial ROS), MitoTracker green (5 μM) or Hoechst (5 μM) for 20 min at 37 °C. Coverslips were then mounted on microscope slides for visualization. Cells on the slides were visualized using a LSM- 900 confocal laser scanning microscope (LSM 900; Carl Zeiss, Oberkochen, Germany), and images were analyzed with the Zen software (Carl Zeiss).

### Immunoblotting assay

Following drug treatment of HT22 cells as indicated, the cells were lysed on ice for 15 min with the RIPA buffer (#P0013B, Beyotime Biotechnology, Shanghai China) containing 1% protease inhibitor cocktail (100×; Selleck Chemicals, Houston, TX, USA). After centrifugation for 15 min at 4 °C at 13,000 *rpm*, the supernatants were mixed with 5× SDS sample buffer (Beyotime Biotechnology, Shanghai, China) and the proteins of interest were separated by electrophoresis with SDS-PAGE. For immunoblot analysis of the dimeric and monomeric forms of iNOS and nNOS, protein samples were prepared with a non-reducing sample buffer without heating [55]. The anti-PDI antibodies (#3501S) were from Cell Signaling Technology (Beverly, MA, USA); the anti-iNOS (#ab178945), anti-nNOS (#ab76067), anti-GPX4 (#ab125066), anti-COX2 (#ab179800) and anti-FACL4 (#ab155282) antibodies from Abcam (Cambridge, MA, USA); the anti-β-actin antibodies (#GB12001 - 100) from ServiceBio (Wuhan, China). The anti-rabbit (#7074S) and the anti-mouse HRP-conjugated secondary antibodies (#7076S) from Cell Signaling Technology (Beverly, MA, USA).

### Cellular thermal shift assay (CETSA)

CETSA was conducted according to the protocols described earlier [56, 57]. Briefly, after the cells were treated with the vehicle or indicated chemicals for 3 h, they were washed with ice-cold PBS, harvested by trypsinization, centrifuged and re-suspended in PBS supplemented with a protease inhibitor cocktail (Selleck Chemicals, Houston, TX, USA). Equal amounts of cell suspensions were aliquoted into 0.2 mL PCR microtubes. Subsequently, aliquots of the cell suspension were heated in a Ristretto Thermal Cycler (VWR, Darmstadt, Germany) at the indicated temperatures for 3 min, followed by cooling for 3 min at room temperature. Finally, the cells were lysed using three cycles of freeze–thawing, and the soluble fractions were isolated by centrifugation and analyzed by SDS-PAGE followed by Western blotting as described above. For isothermal dose-response CETSA ($\mathrm{ITDR}_{\mathrm{CETSA}}$), the fold of change in PDI (which is normalized to the β-actin control) is plotted as a function of temperature to generate the PDI melting curve for selected treatments.

### siRNA transfection assay

For siRNA transfection, the siRNAs (60 nM) for the target gene *PDI* were transfected into HT22 cells with Lipofectamine RNA iMAX (Invitrogen) at 24 h after seeding.

Twenty-four h following siRNA transfection, cells were treated with respective drugs, and subsequently processed for cell viability measurement and immunoblot analysis. The siRNA sequences targeting the mouse PDI (siPDIs) are CCAAGTACCAGCTGGACAA (#1), GAACGGTCATTGATTACAA (#2), and TGCTAAGATGGACTCAACA (#3), and these three siRNA sequences were evenly mixed to maximize transfection efficiency.

### Protein expression and purification

The mutant PDI-Ala256 protein was prepared from the full-length wild-type human PDI-His256 cDNA using the QuikChange II XL Site-Directed Mutagenesis Kit (Agilent Technologies). For protein purification, PCR products of the wild-type PDI-His256 and the mutant PDI-Ala256 were subcloned into pET28a, and the proteins were expressed in the *E. coli* strain JM109 (DE3) cultured in Luria-Bertani (LB) medium. After the bacteria were cultured at 37 °C to reach an OD value of approximately 0.8, then 1 mM isopropyl-β-*D*– 1-thiogalactopyranoside (IPTG) was added into LB medium, and the bacteria were further cultured at 22 °C for 8 h. The bacteria were harvested by centrifugation at 5000 × g for 30 min at 4 °C, and lysed in the presence of a protease inhibitor cocktail. The supernatant was isolated by centrifugation at 20,000 × g for 30 min and then incubated with Ni-NTA agarose (QIAGEN) at 4 °C for 1 h. The columns were washed and eluted with 20 mM imidazole. The proteins were concentrated and analyzed by SDS-PAGE.

### Assay of PDI catalytic activities and the inhibition by BAZ

PDI has both reductase activity (*i.e.*, the reduction of a disulfide bond in protein substrates to two free thiol groups) and oxidase activity (*i.e.*, the conversion of two free thiol groups in protein substrates to form a disulfide bond). The reductase activity of PDI was determined by analyzing PDI-mediated aggregation of the insulin B chain as described earlier with some modifications [58, 59]. Briefly, insulin (125 μM) was incubated in a 96-well plate in 10 mM sodium phosphate buffer (pH 7.4) and 5 mM DTT with or without the recombinant PDI protein (at approximately 0.2 μg/μL). The aggregation was monitored at 37 °C using a Synergy Plate Reader (Biotek, Winooski, VT, USA) with wavelength set at 650 nm. The oxidase activity of PDI was assessed using the RNase A refolding assay [58, 60]. Briefly, 5-mg RNase A was dissolved in a buffer containing 6 M urea and 140 mM DTT and incubated overnight at 4 °C to induce denaturation. Urea and DTT were then removed by dialysis, yielding partially folded RNase A. The refolding reaction mixture contained 1.2 mM GSH, 0.2 mM GSSG, 8 μM denatured RNase A, and 4.5 mM cyclic CMP, with or without the addition of the recombinant PDI protein (at approximately 0.1 μg/μL). Absorbance changes were monitored at 296 nm using a Synergy Plate Reader (Biotek) at 37 °C.

### Molecular docking analysis

The PDI–ligand interaction was analyzed using the molecular docking method. The experimental structures of reduced human PDI (PDB code 6I7S, chain A) [61], oxidized human PDI (PDB code 4EL1, chain A) [62] and BAZ (extracted from the ER–BAZ complex; PDB code 6PSJ, ligand ID 29S) [63] were downloaded from the Protein Data Bank (https://www.rcsb.org/) [64] and adopted as the receptor and ligand, respectively. The missing residues in the experimental structures (PDB code 4EL1, chain A, residues 250–254, 320–323) were added using SWISS-MODEL (https://swissmodel.expasy.org/), a web server for structure prediction using homology modeling [65]. The 3 possible ligand binding sites on the structures of human PDI predicted in our recent study [66] were used for BAZ docking to predict the structures of PDI–BAZ complexes.

The structures were processed using the Protein Preparation Wizard in Schrodinger Suite (Maestro 12.8, 2021; Schrodinger LLC, New York, NY, USA). The hydrogen atoms were added, and the protein structures were optimized using OPLS4 force field [67]. The protein–ligand docking decoys were generated using Glide-XP (extra precision) in Schrodinger Glide software [68]. The nearby torsional minima of the lowest energy binding poses were sampled using Monte Carlo (MC) procedure. Each geometric center of the predicted ligand binding site of PDI was used as the center of the docking grid box with dimensions set at 36 × 36 × 36 $Å^3$.

Lastly, three representative scoring functions, X-Score [69], PRODIGY-LIG [70] and $\Delta_{vina}RF_{20}$ [71] were employed for further filtering of the docking results. The two linear empirical scoring functions, *i.e.*, X-Score [69] and PRODIGY-LIG [70], were developed for calculating protein–ligand binding affinity. The former employs energy and geometric terms such as *van der Waals* energy, hydrogen bonding energy, deformation penalty and hydrophobic effect [69], and the latter uses the number of atomic contacts and electrostatic energy [70]. $\Delta_{vina}RF_{20}$ is a random forest-based method for binding affinity prediction based on 20 descriptors [71].

To investigate the importance of His256 in the interactions between PDI and BAZ, His256 was mutated to alanine (Ala) in the representative predicted structures of the PDI–BAZ complex. The binding energies were predicted using X-Score [69], PRODIGY-LIG [70] and $\Delta_{vina}RF_{20}$ [71].

## Molecular dynamics simulations

The stability of the binding poses of BAZ in the predicted structures of PDI–BAZ complex was investigated using molecular dynamics (MD) simulations. The complexes were processed using CHARMM-GUI (https://charmm-gui.org/) to generate the topology files [72]. The force field parameters of BAZ were generated based on CHARMM general force field [73], those of protein were generated based on CHARMM36 m force field [74]. The systems were embedded into a rectangular water box extending the solvent 10 Å in *x*, *y*, *z* directions, and the TIP3P water model [75] was used. $K^+$ and $Cl^-$ ions with parameters approximated by Roux *et al.* [76] were added to neutralize the charges of the systems. The energy minimization (10000 steps), equilibrium simulation (0.25 ns) in NVT ensemble and production simulation (100 ns) in NPT ensemble were carried out using NAMD [77]. The time step and temperature were set to 2 fs and maintained at 300 K using Langevin dynamics [78], respectively. The periodic boundary conditions were employed, the short-range electrostatic and *van der Waals* interactions were truncated smoothly with a cutoff (12 Å) and a switching function was employed at 10 Å. Long-range electrostatic interaction was estimated by the particle mesh Ewald algorithm [79, 80]. The pressure in NPT ensemble was maintained at 1 atm by the Langevin piston method [81]. The number of hydrogen bonds formed between BAZ and PDI and the contact number and binding energies between BAZ and PDI in the representative conformations along the MD trajectories were calculated to confirm the importance of His256 and the stability of the predicted binding poses.

## *In vivo* animal experiments and drug treatments

The procedures involving the use of live animals described in this study were approved by the Institutional Animal Care and Use Committee (IACUC) of The Chinese University of Hong Kong (Shenzhen), and the guidelines for humane care of animals set forth by the U.S. National Institutes of Health were followed. Male mice (6–8 weeks of age), weighing 20–30 g, were purchased from Guangdong Charles River Laboratories (Beijing, China). After arrival, the animals were allowed to acclimatize to the new environment for one week before they were used in experimentation. Mice were randomly divided into different experimental groups ($n = 6$–$8$) with comparable average body weights. Male mice were used in this study because female mice normally produce and secrete large amounts of endogenous estrogens in a cyclic fashion (depending on their estrous cycle), and our earlier study has shown that the endogenous estrogens and some of their derivatives have a protective effect against neuronal cell death [82]. Therefore, the use of male mice would help minimize this endogenous confounding factor.

Kainic acid (3 μL of 0.2 mM solution in saline) was injected into the left and right lateral ventricles using a microliter syringe under anesthesia with Zoletil50 and xylazine (50 and 5 mg/kg, *i.p.*), and the control mice were injected with 3 μL of vehicle (saline) without kainic acid. The bilateral intracerebroventricular (*i.c.v.*) injection parameters were: anterior/posterior, −0.5; rostral, ± 1.1; and dorsal/ventral, 2.7. The animals were also given *i.p.* injection of a solution (100 μL) containing 0.375, 0.75 or 1.25 mg/mL of BAZ (the solvent is 10% DMSO + 90% corn oil) once every 2 days. The three BAZ doses approximately equal to 1.5, 3 or 5 mg/kg of body weight. The first dose of BAZ was given 24 h before *i.c.v.* injection of kainic acid, and the treatment lasted for 11 days. Note that in this study, the control animals were sham-operated (receiving *i.c.v.* injection of 3 μL saline solution) and also received *i.p.* injections of 100 μL vehicle (containing 10% DMSO and corn oil). For kainic acid alone group, the animals received *i.p.* injections of 100 μL vehicle (10% DMSO and corn oil); for the BAZ alone group, the animals were sham-operated (receiving *i.c.v.* injection of 3 μL saline solution).

## Memory and learning ability tests

The first test used in this study was the classical Y-maze-based method which was intended to determine the degree of memory impairments in mice following different treatments [83, 84]. The test started 6 days after *i.c.v.* injection of kainic acid. The Y-maze (made of polyvinyl plastic) was a three-arm maze with equal angles between the three arms (30 cm in length, 5 cm in width, and 15 cm in wall height). As depicted in Fig. 9B, the test animals were initially placed at the end of one arm, and the sequence and number of arm entries were recorded manually. Based on earlier studies [83, 84], the percentage of trials with all three arms represented, *i.e.*, ABC, CAB or BCA (but not ABA, BAB or CBC), was recorded as an alternation for estimation of the short-term memory. Arms were cleaned between tests with 70% ethanol-containing paper towels to remove odors and residues. The alternation score (%) for each mouse is defined as the ratio of the actual number of alternations to the possible number (defined as the total number of arm entries minus two) multiplied by 100 as in the following equation [85]:

$$\%\ \text{alternation} = [(\text{number of alternations})/(\text{total arm entries} - 2)] \times 100$$

In this study, a new Y-maze-based test was also developed in our laboratory to further evaluate the learning ability and the degree of memory impairments of the same animals. In this method, all tests started from day 10 post *i.c.v.* injection of kainic acid (see Fig. 9A), and all mice, including the control mice, were food restricted starting 24 h before the test, receiving on average 2–3 g pellet food only. As depicted in Fig. 9B, in one of the arms the animal food was placed as a bait. The animal was placed in the starting arm, and then it was allowed to freely explore the Y-maze to find the food (which was placed at the end of another arm) and ate it. Then, the animal was placed back at the same starting place and the observation was repeated again. If the animal went straight to where the food was originally placed and ate the food, it was considered that the animal remembered correctly where the food was. In order to evaluate how well the learning ability and memory of each animal, the number of wrong entries the animal made during the initial 20 trials (10 trials per day, in two consecutive days) and the amount of time the animal took to find and start to eat the food in every trial were recorded. To minimize the random variations in each individual trial, the first three consecutive trials (*i.e.*, trials 1–3) were combined to calculate the average value as the first recording, the next three consecutive trials (*i.e.*, trails 4–6) were combined to calculate the average value for the second recoding, and the same method was applied to calculate other recording values. The last two trials (*i.e.*, trials 19 and 20) were combined to calculate the average value for the last recording.

### Histochemical and fluorescence staining of the brain sections

To perform histochemical and fluorescence staining of the brain sections to determine the degree of brain damage in different treatment groups, separate groups of animals were sacrificed on day 6 post *i.c.v.* injection of kainic acid. Prior to collecting the brain tissues from the animals for analysis, the animals received ketamine and xylazine (50 and 5 mg/kg, *i.p.*) for anesthesia, and then they were perfused with physiological saline (0.9% NaCl) and 4% paraformaldehyde via the abdominal aorta. The collected brain tissues were fixed overnight in 4% paraformaldehyde. After cryoprotection in 30% sucrose/phosphate buffer, the whole brain tissues were frozen in liquid nitrogen and sectioned serially (in 30-μm thickness). Brain sections were collected in 0.1 M neutral phosphate buffer, mounted on slides, then air-dried on a slide warmer at 50 °C for at least 0.5 h, and stained with hematoxylin and eosin (H/E) for histological analysis. Three brain hippocampal regions (CA1, CA3 and the dentate gyrus DG) were examined bilaterally as described earlier [82].

The apoptotic DNA degradation in brain tissue slides was determined using the terminal deoxynucleotidyl transferase (TdT)-mediated dUDP-biotin nick end labeling (TUNEL) method according to supplier's instructions (Biosharp, China). The Fluoro-Jade B staining was performed according to supplier's instructions (Biosensis, Australia). Briefly, the slides were transferred to a solution of 0.06% potassium permanganate for 10 min on a shaker. The Fluoro-Jade B staining solution was prepared from the 0.1-mg/mL stock solution (in distilled water). After 10 min in the staining solution, the slides were rinsed and placed on a slide warmer until they were dry. Images were captured with a light microscope (Carl Zeiss Corporation, Germany) and cell counting was performed using the ImageJ software.

### Statistical analysis

Most of the quantitative measurements were repeated multiple times to confirm the experimental observations reported in this study. The quantitative data were usually presented as mean ± S.D. based on multiple replicate measurements from a selected experiment. Statistical analyses were carried out using one-way or two-way ANOVA as needed, followed by Dunnett's post-hoc tests for multiple comparisons (GraphPad Prism 10.0 software; GraphPad Software, La Jolla, CA). Statistical significance was denoted by $P < 0.05$ ($^{*}$ or $^{\#}$) and $P < 0.01$ ($^{**}$ or $^{\#\#}$) for significant and very significant differences, respectively. In most cases, $^{*}$ and $^{**}$ denote the comparison for statistical significance between the control group (cells treated with the vehicle only) and the cells treated with a cell death inducer (such as erastin or RSL3), whereas $^{\#}$ and $^{\#\#}$ denote the comparison between the cells treated with the cell death inducer alone and the cells jointly treated with the cell death inducer plus a modulating compound (such as BAZ).

## Results

### BAZ prevents erastin-induced ferroptosis and NO/ROS accumulation

#### *Ferrotosis protection*

Based on changes in gross morphology and cell viability (MTT assay), treatment of HT22 mouse hippocampal neuronal cells with erastin readily induced cell death in a dose-dependent manner (Fig. 1B). Joint treatment of these cells with BAZ (from 125 to 2000 nM) abrogated erastin-induced cell death in a concentration-dependent manner (Fig. 1C). The protective efficacy of BAZ was very high as 100% protection was readily observed when 500 nM BAZ was present (Fig. 1C). Further analysis confirmed that BAZ effectively attenuated cell death when the live and dead cells were analyzed using Calcein AM/PI double staining (Fig. 1D).

We have also determined, for comparison, the protective effects of BAZ against erastin-induced cell death in three additional cell lines, *i.e.*, the ER-negative

MDA-MB- 231 human breast cancer cells, the BRL- 3 A rat hepatocytes, and the H9 C2 rat cardiomyocytes. We found that BAZ exerted a complete protection against erastin-induced cell death in these cells (Supplementary Fig. S1 A−S1 C).

In this study, we performed RT-qPCR analysis to assess the mRNA levels of key representative ferroptosis markers and Western blot analysis to evaluate their protein levels in HT22 cells treated with erastin ± BAZ. It was observed that while erastin exposure reduced the levels of *GPX4* mRNA (Fig. 1E) and its protein (Fig. 1H), it increased the levels of *PTGS2* and *ACSL4* mRNAs (Fig. 1F, G) and their protein levels (COX2 and FACL4, respectively; Fig. 1H). These changes are characteristic for erastin-induced ferroptotic cell death. Joint treatment of cells with BAZ abrogated erastin-induced changes in three of the ferroptosis markers (Fig. 1E−H).

### *NO and ROS accumulation*

Our recent studies have shown that erastin-induced ferroptosis in HT22 cells is associated with sequential accumulation of cellular NO, ROS and lipid-ROS [32]. By using fluorescence microscopy and flow cytometry analyses, we confirmed that erastin caused accumulation of cellular NO (DAF-FM-DA as a probe) in a time-dependent manner in HT22 cells (Supplementary Fig. S2 A−S2 C), and NO accumulation in erastin-treated cells was abrogated by joint treatment of these cells with 1 μM BAZ (Fig. 1I, Supplementary Fig. S3).

$ONOO^-$ is a reactive toxic metabolite of NO which can be formed in the cells [86]. In this study, we also determined the change in cellular $ONOO^-$ levels (using O58 as a probe) in erastin-treated cells. We found that erastin caused a time-dependent increase in cellular $ONOO^-$ levels (Supplementary Fig. S4 A), and its buildup was effectively abrogated by joint treatment with BAZ (Supplementary Fig. S4B). Similarly, urea, a weak scavenger of $ONOO^-$, partially abrogated erastin-induced $ONOO^-$ buildup (Supplementary Fig. S4 C), however, urea did not exhibit any cytoprotective effect against erastin-induced cytotoxicity (Supplementary Fig. S4D).

Erastin also caused the accumulation of cellular ROS (DCFH-DA as a probe, Supplementary Fig. S5) and lipid-ROS (C11-BODIPY as a probe, Supplementary Fig. S6) in a time-dependent manner, and their accumulation was effectively abrogated by BAZ (Fig. 1J, Supplementary Fig. S7 for ROS; Fig. 1K, L, Supplementary Fig. S8 for lipid-ROS). In addition, erastin-induced accumulation of mitochondrial ROS (MitoSOX as a probe) was also similarly reduced by treatment with BAZ (Fig. 1M, Supplementary Fig. S9). Interestingly, substantial aggregation of mitochondrial ROS was observed in the nucleus of erastin-treated cells. Notably, nuclear aggregation of mitochondrial ROS typically occurs during late stages of ferroptosis, and this phenomenon was also observed in other cell lines [87]. BAZ completely abrogated mitochondrial ROS accumulation inside the nucleus (Fig. 1M, Supplementary Fig. S9).

In summary, these results indicate that BAZ has a strong protective effect against erastin-induced ferroptosis in HT22 neuronal cells. In addition, BAZ has the unique ability to broadly attenuate cellular NO, ROS, lipid-ROS and mitochondrial ROS levels in erastin-treated HT22 cells.

## BAZ protects against RSL3-induced ferroptosis and NO/ROS accumulation

### *Ferroptosis protection*

We have also determined in this study the protective effect of BAZ against RSL3-induced ferroptotic cell death. While treatment of cells with RSL3 alone elicited a concentration-dependent loss of cell viability (Fig. 2A), a strong protection against RSL3-induced cell death was observed when the cells were jointly treated with BAZ (Fig. 2B), and 100% protection was seen when 250 nM BAZ was present. It is evident that the protective effect of BAZ against RSL3-induced cell death has a higher potency than its protection against erastin-induced ferroptosis. Additional experiments using Calcein AM/PI double staining confirmed that BAZ effectively rescue cells from RSL3-induced cytotoxicity (Fig. 2C). Similar to the observations made with erastin, a strong protection

(See figure on next page.)

**Fig. 2** BAZ protects against RSL3-induced ferroptosis. **A**, **B**. Cytotoxicity of RSL3 alone (**A**) and its protection by BAZ (**B**) after 24-h treatment with RSL3 ± BAZ at indicated concentrations (MTT assay, *n* = 5). **C**. Calcein-AM/PI double staining of live and dead cells following 8-h treatment with 0.08 μM RSL3 ± 1 μM BAZ (fluorescence microscopy images, scale bar = 60 μm). **D**–**F**. mRNA levels of *GPX4* (**E**), *PTGS2* (**F**) and *ACSL4* (**G**). Cells were treated with 0.08 μM RSL3 ± 1 μM BAZ for 2 h (for detection of *PTGS2*) or 8 h (for detection of *GPX4* and *ACSL4*), and then their mRNA levels were determined by RT-qPCR (*n* = 3). **G**. Cellular levels of GPX4, COX2 and FACL4 proteins after 8-h treatment with 0.08 μM erastin ± 1 μM BAZ (Western blotting). **H**–**J**. Cellular levels of NO (**H**), ROS (**I**) and lipid-ROS (**J**) after 8-h treatment with 0.08 μM RSL3 ± 1 μM BAZ (analytical flow cytometry). The left panels of **H**, **I**, **J** are the histograms, and the right panels are respective quantitative intensity values (*n* = 3). **K**. Cellular levels of lipid-ROS after 8-h treatment with 0.08 μM RSL3 ± 1 μM BAZ. The cells were stained with BODIPY and Hoechst, and then subjected to confocal microscopy ( scale bar = 10 μm). **L**. Levels of mitochondrial ROS after 8-h treatment with 0.08 μM RSL3 ± 1 μM BAZ. The cells were stained with MitoSOX, MitoTracker and Hoechst, and then subjected to confocal microscopy (scale bar = 10 μm). Quantitative data are presented as mean ± S.D. (* or $^{\#}$ $P < 0.05$; ** or $^{\#\#}$ $P < 0.01$)

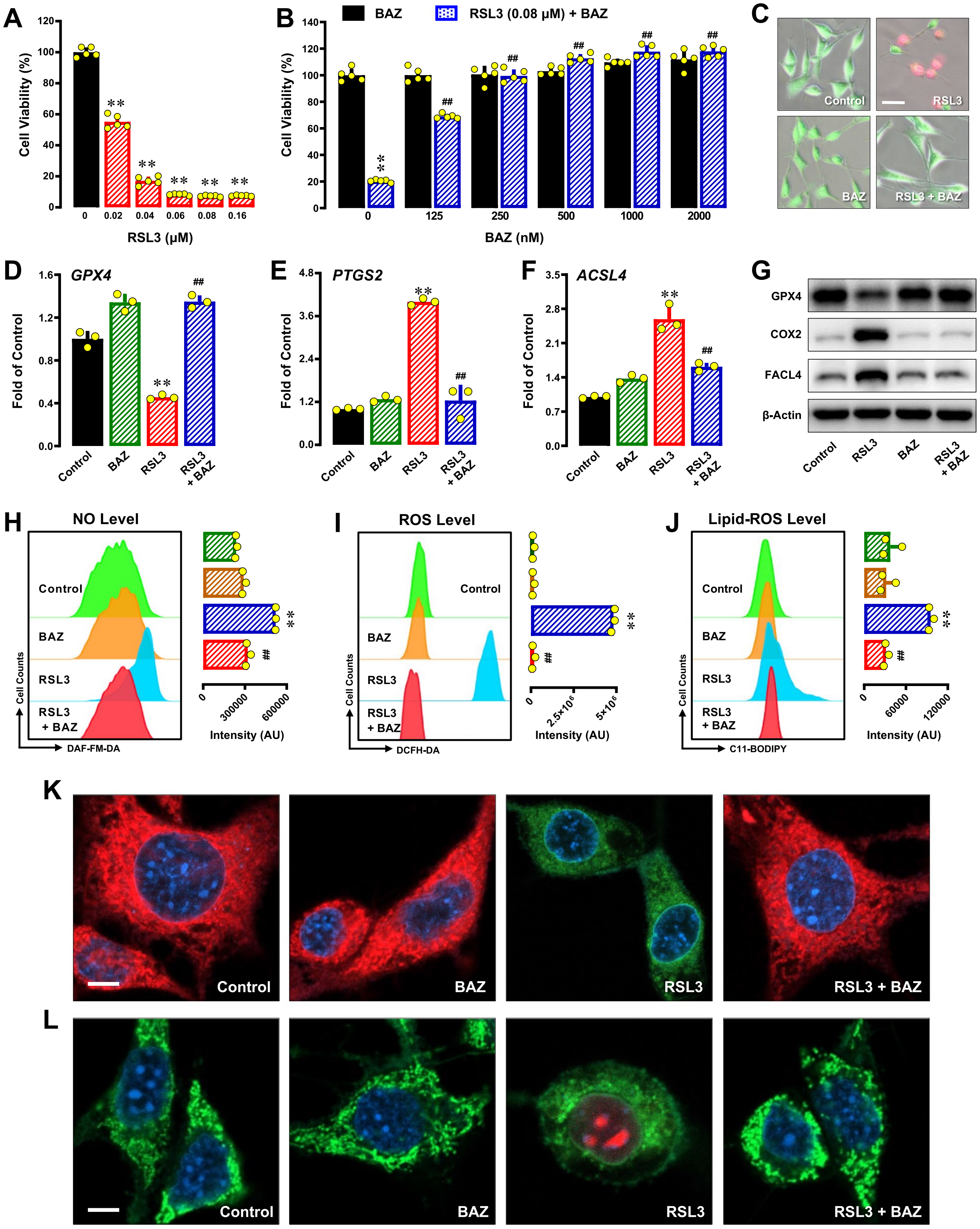

**Fig. 2** (See legend on previous page.)

by BAZ against RSL3-induced cell death was also observed in MDA-MB- 231, BRL- 3 A and H9 C2 cells (Supplementary Fig. S10 A–S10 C).

It was observed that while RSL3 decreased the levels of *GPX4* mRNA and its protein in HT22 cells (Fig. 2D, G), it increased the levels of *PTGS2* and *ACSL4* mRNAs (Fig. 2E, F) and their protein levels (COX2 and FACL4, respectively; Fig. 2G). Joint treatment of cells with BAZ abrogated RSL3-induced changes in these mRNAs and proteins (Fig. 2D–G).

#### *Effect on NO and ROS accumulation*

We also determined the effect of BAZ on RSL3-induced accumulation of cellular NO, ROS/lipid-ROS and mitochondrial ROS. We found that RSL3 increased the cellular levels of NO in a time-dependent manner (Supplementary Fig. S11 A–S11 C), and the presence of 1 μM BAZ effectively abrogated RSL3-induced NO accumulation (Fig. 2H, Supplementary Fig. S12). Treatment of HT22 cells with RSL3 also caused time-dependent accumulation of cellular ROS (Supplementary Fig. S13) and lipid-ROS (Supplementary Fig. S14). RSL3-induced accumulation of cellular ROS (Fig. 2I, Supplementary Fig. S15) and lipid-ROS (Fig. 2J, K, Supplementary Fig. S16) was similarly abrogated by BAZ. Additionally, RSL3-induced accumulation of mitochondrial ROS and its aggregation in the nucleus was also abrogated by BAZ (Fig. 2L, Supplementary Fig. S17).

Here, it is of note that the cellular levels of $ONOO^-$ (detected using O58 as a probe) were found to be increased in a time-dependent manner in RSL3-treated cells (Supplementary Fig. S18 A), and its buildup was effectively abrogated by joint treatment with BAZ (Supplementary Fig. S18B). While urea modestly reduced RSL3-induced $ONOO^-$ accumulation (Supplementary Fig. S18 C), it did not display any protective effect against RSL3-induced cell death (Supplementary Fig. S18D).

In summary, these results indicate that BAZ has an exceptionally strong protective effect against RSL3-induced ferroptosis in HT22 cells through attenuation of the accumulation of cellular NO, ROS/lipid-ROS, and mitochondrial ROS.

### Biochemical analysis of BAZ binding with PDI

The above observations prompted us to identify the cellular target that mediates the cytoprotective effect of BAZ. Our recent studies have shown that PDI is a cellular protein that can mediate chemically-induced oxidative cell death [31]. Next, we sought to determine whether PDI is a cellular protein that also mediates the protective effect of BAZ against chemically-induced ferroptosis in HT22 cells. As summarized below, a series of experiments were performed.

We first determined the binding affinity of BAZ with PDI using the surface plasmon resonance assay, and found that BAZ can bind to PDI with a very high binding affinity (apparent $K_d = 3.3$ nM based on curve fitting and 3.6 nM based on Scatchard plot) (Fig. 3A, B).

Next, we performed the cellular thermal shift assay (CETSA) to evaluate whether BAZ can bind to PDI proteins in live HT22 cells. Based on Western blot analysis of PDI protein stability, a thermal shift associated with PDI protein was observed in BAZ-treated HT22 cells compared to the control cells (Fig. 3C). A change in the $Tm_{50}$ values (the temperature at which 50% of the proteins are precipitated by thermal denaturation) was determined to reflect the direct binding interaction of PDI protein with BAZ in live HT22 cells in culture. PDI had a $Tm_{50}$ value of 56.5 °C in control cells (in the absence of BAZ), but the presence of BAZ increased its $Tm_{50}$ to ~ 60 °C, resulting in an increase in the $Tm_{50}$ value (*i.e.*, $\Delta Tm_{50}$) by 3.5 °C (Fig. 3E).

To provide further support for the above experimental observations, the isothermal dose-response CETSA ($ITDR_{CETSA}$) was also performed. The isothermal stability of PDI treated with different doses of BAZ at 59 °C showed that PDI protein in HT22 cells was stabilized by the presence of BAZ in a concentration-dependent manner (Fig. 3D). The CETSA curve nearly reached the plateau when 32 μM of BAZ was present (Fig. 3F). Together, these results show that BAZ can bind to PDI proteins in live HT22 cells.

### BAZ inhibits PDI's catalytic activities

PDI has both reductase and oxidase activities, which catalyze the isomerization between free thiol groups

(See figure on next page.)

**Fig. 3** Binding of BAZ to PDI protein in live HT22 cells in culture. **A**, **B**. Surface plasmon resonance analysis of the binding affinity of BAZ for the purified wild-type PDI-His256 protein (**A** for the concentration-dependent binding curve; **B** for Scatchard plot analysis based on the data in **A**). **C**. CETSA analysis of the change in PDI thermostability in 10 μM BAZ-treated intact cells in response to increasing temperatures (*n* = 3). **D**. $ITDR_{CETSA}$ analysis of the change in PDI thermostability in intact cells at 59 °C in the presence of increasing concentrations of BAZ. **E**. Relative intensities of the protein bands in panel **C** after quantified using the Image J software. For CETSA curves, the relative band intensities are calculated according to the intensities at the lowest temperature for the BAZ-exposed samples and control samples, respectively (*n* = 3). **F**. Relative intensities of the protein bands in panel **D** after normalized to the β-actin samples (*n* = 3). Quantitative data are presented as mean ± S.D. (** $P < 0.01$)

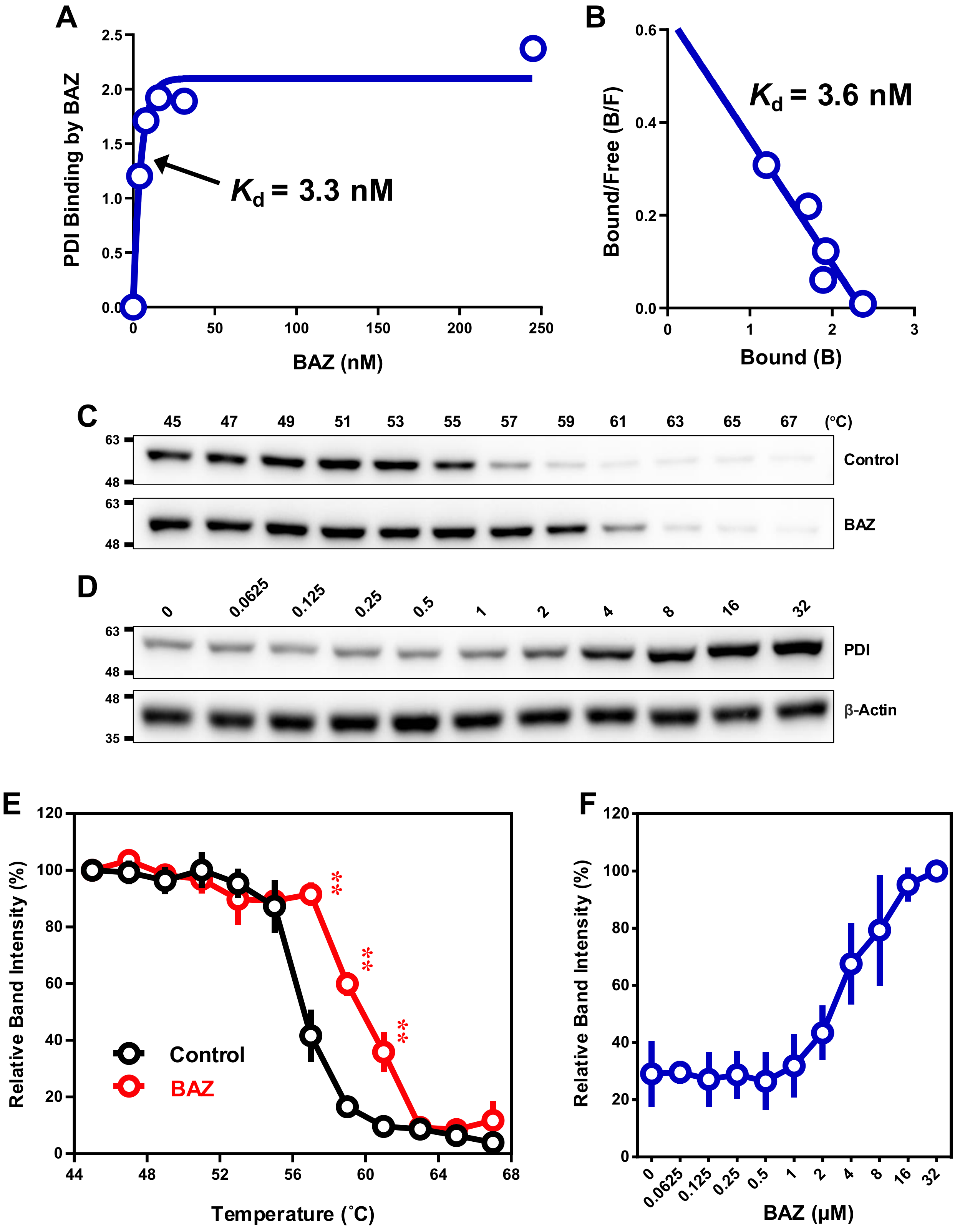

**Fig. 3** (See legend on previous page.)

and disulfide bonds in cellular target proteins. Results from our recent studies have shown that PDI-mediated NOS dimerization (*i.e.*, formation of a disulfide bond between two NOS monomers) plays a crucial role in mediating chemically-induced oxidative ferroptosis [32, 33, 54]. Therefore, we determined in this study the modulating effect of BAZ on the reductase and oxidase activities of PDI using *in vitro* enzymatic assays.

First, we determined whether BAZ can directly inhibit PDI's reductase activity by using the *in-vitro* insulin aggregation assay [58]. We found that the reductase activity of the wild-type PDI-His256 protein was effectively inhibited by the presence of BAZ in a concentration-dependent manner (Fig. 4A); in contrast, BAZ failed to similarly inhibit the reductase activity of the mutant PDI-Ala256 (Fig. 4B). While the mutant PDI-Ala256 protein appeared to have a slightly-reduced catalytic velocity (*i.e.*, it took slightly longer to produce the same levels of insulin aggregation), its ability to complete the same levels of maximal reaction was not altered (compare Fig. 4A and B).

We also determined whether BAZ directly inhibits PDI's oxidase activity using the *in-vitro* RNase A refolding assay. We found that BAZ effectively inhibited the oxidase activity of the wild-type PDI-His256 protein in a concentration-dependent manner (Fig. 4C). Interestingly, BAZ also exhibited similar levels of inhibition of the oxidase activity of the mutant PDI-Ala256 protein (Fig. 4D), which is different from its inability to inhibit the reductase activity of the mutant PDI-Ala256 protein.

### Computational modeling of PDI–BAZ binding interactions

Computational analyses were employed to help better understand the experimental results on PDI–BAZ interactions and BAZ's inhibition of PDI enzyme activities. According to our selection criteria that the docking structures need to be ranked at least by two of the three scoring functions in the top 20, there are 15 representative structures selected from 202 docking decoys for the oxidized PDI–BAZ complexes. Among these 15 structures for the oxidized PDI–BAZ complex, they include three binding sites (Fig. 5A, Table 2). The binding site 1 is located between the *a'* and *b'* domains and has 5 structures; a representative structure (#1) is shown in Fig. 5B, C. The binding of BAZ to binding site 1 of the oxidized PDI would interfere with the relative movements between the *a'* and *b'* domains of the oxidized PDI as compared to its structure in the absence of BAZ. It is believed that the relative movements between different domains are important for PDI to perform its normal catalytic functions. The binding site 2 is located in the *a* domain (near the active site) and has 4 structures; a representative structure (#6) is shown in Fig. 5D, E. The binding site 3 is located in the *a'* domain (also near the active site) and has 6 structures; a representative structure (#10) is shown in Fig. 5F, G. The binding of BAZ to binding sites 2 and 3 of the oxidized PDI will directly affect the binding of the substrate proteins to the active sites of the oxidized PDI, which are expected to inhibit its catalytic activity. Since BAZ does not make direct interactions with His256 in the *b'* domain of the oxidized PDI, the His256 Ala mutation is not expected to affect the interactions of BAZ with the oxidized PDI. This prediction is in agreement with our experimental results, as His256 mutation does not affect PDI's oxidase activity.

Next, we also investigated the binding interactions of BAZ with the reduced PDI. Seven predicted structures for the reduced PDI−BAZ complexes are selected (Fig. 6A, Supplementary Fig. S19 A−S24 A). BAZ interacts closely with the *b'* domain of the reduced PDI and forms a hydrogen bond with His256 (Fig. 6B, Supplementary Fig. S19B−S24B). When PDI's His256 is mutated to Ala256, the hydrogen bond between BAZ and His256 disappears (Fig. 6D, Supplementary Fig. S19D−S24D). The surfaces of the binding pockets are shown in Fig. 6C and E (Supplementary Fig. S19 C−S24 C, S19E−S24E). The differences in the binding pockets of the wild-type and mutant PDI proteins are mostly in the regions surrounding His256 which is a basic amino acid and mutated to a nonpolar amino acid (Ala256). The predicted binding affinities based on the 7 representative structures are summarized in Table 3. The binding energy values are increased after the His→Ala mutation, indicating that the stability of the binding interactions between PDI and BAZ are decreased by the mutation.

Next, MD simulations were performed to probe how well BAZ binds to the reduced PDI-His256 and PDI-Ala256. In the case of the wild-type PDI-His256, it is observed that BAZ still remains bound to PDI's His256 in two of the three MD simulations (Fig. 7A, B), but BAZ dissociates from His256 in one of the MD simulations (Fig. 7C). In comparison, for the mutant PDI-Ala256, BAZ dissociates from Ala256 in all three MD simulation trajectories (Fig. 7G, H, I).

It is of interest to see that after MD simulation, the conformation of the wild-type PDI-His256 is changed from its initial open state (as shown in Fig. 6A) to the closed state (Fig. 7A) or partially-closed state (Fig. 7B). Similar observations are also made with the mutant PDI-Ala256, which is changed from its initial open state to closed-state (Fig. 7H) and then to partially-closed state (Fig. 7G, I).

After MD simulation, the aromatic ring of BAZ remains buried inside the binding pocket of the wild-type PDI-His256, whereas the other part of the BAZ molecule is rotated (Figs. 6B, C, and 7D, E). The contact number between BAZ and PDI-His256 (atom pairs within a given

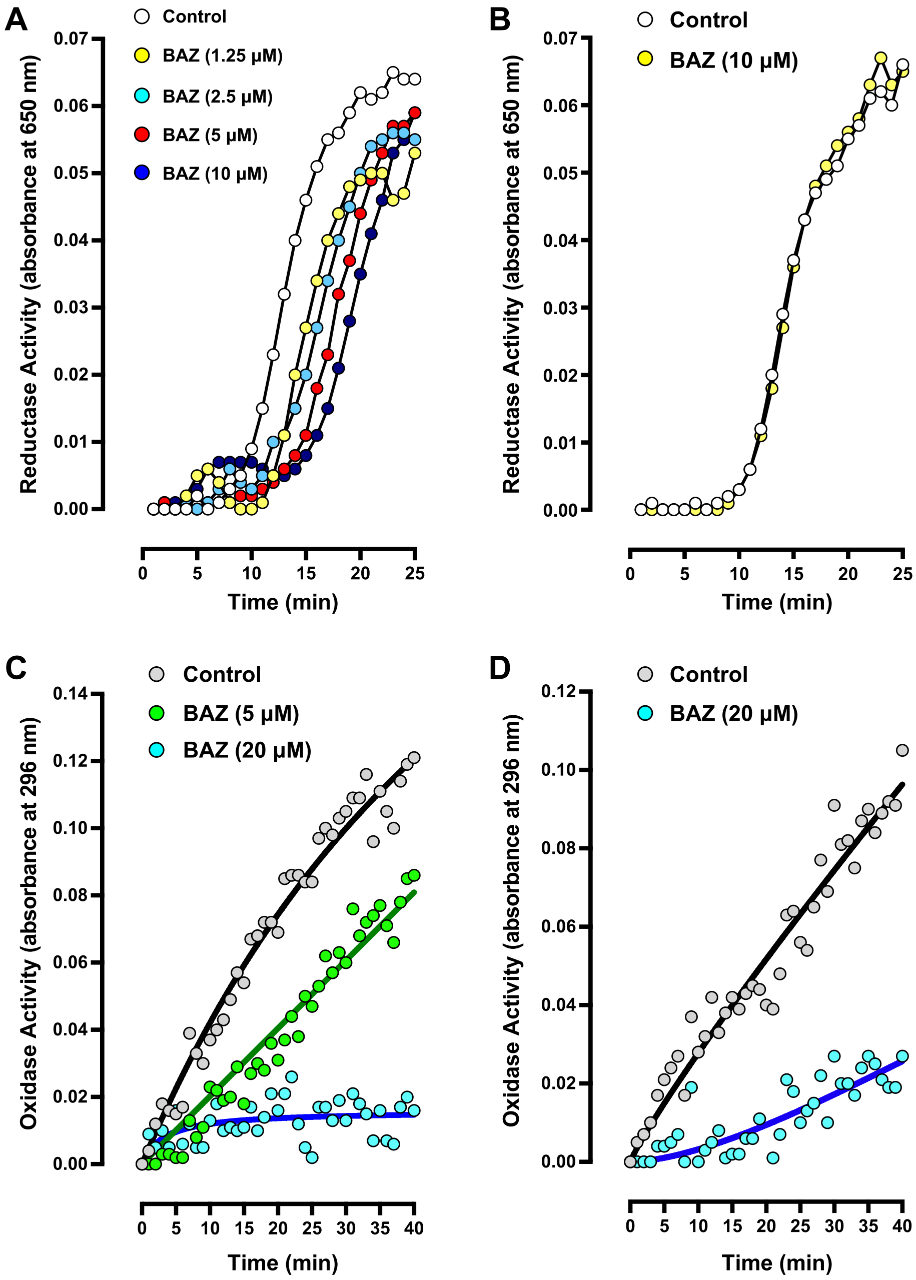

**Fig. 4** Effect of BAZ on the reductase and oxidase activity of PDI in the *in-vitro* enzymatic assays. **A**, **B**. Inhibition by BAZ of the reductase activity of the wild-type PDI-His256 (**A**) and mutant PDI-Ala256 (**B**). The reductase activity of PDI was assayed by measuring PDI-mediated insulin aggregation. The assay was repeated three times and similar results were obtained. The data from a representative assay is shown here. **C**, **D**. Inhibition by BAZ of the oxidase activity of the wild-type PDI-His256 (**C**) and mutant PDI-Ala256 (**D**). The oxidase activity of PDI was assayed by measuring PDI-mediated RNase A refolding. The assay was repeated three times and similar results were obtained. The data from a representative assay is shown here

cutoff of 5 Å) is shown in Supplementary Fig. S25 A. The atomic contact number in the wild-type PDI-His256–BAZ complex (Supplementary Fig. S25 A) along two of the three MD trajectories fluctuates around 800 during the simulation process, and the contact number in the mutant PDI-Ala256–BAZ complex along two of the three MD trajectories nearly goes down to zero after 40-ns MD simulation. While the minimum distance between BAZ and PDI-Ala256 becomes very long in the mutant

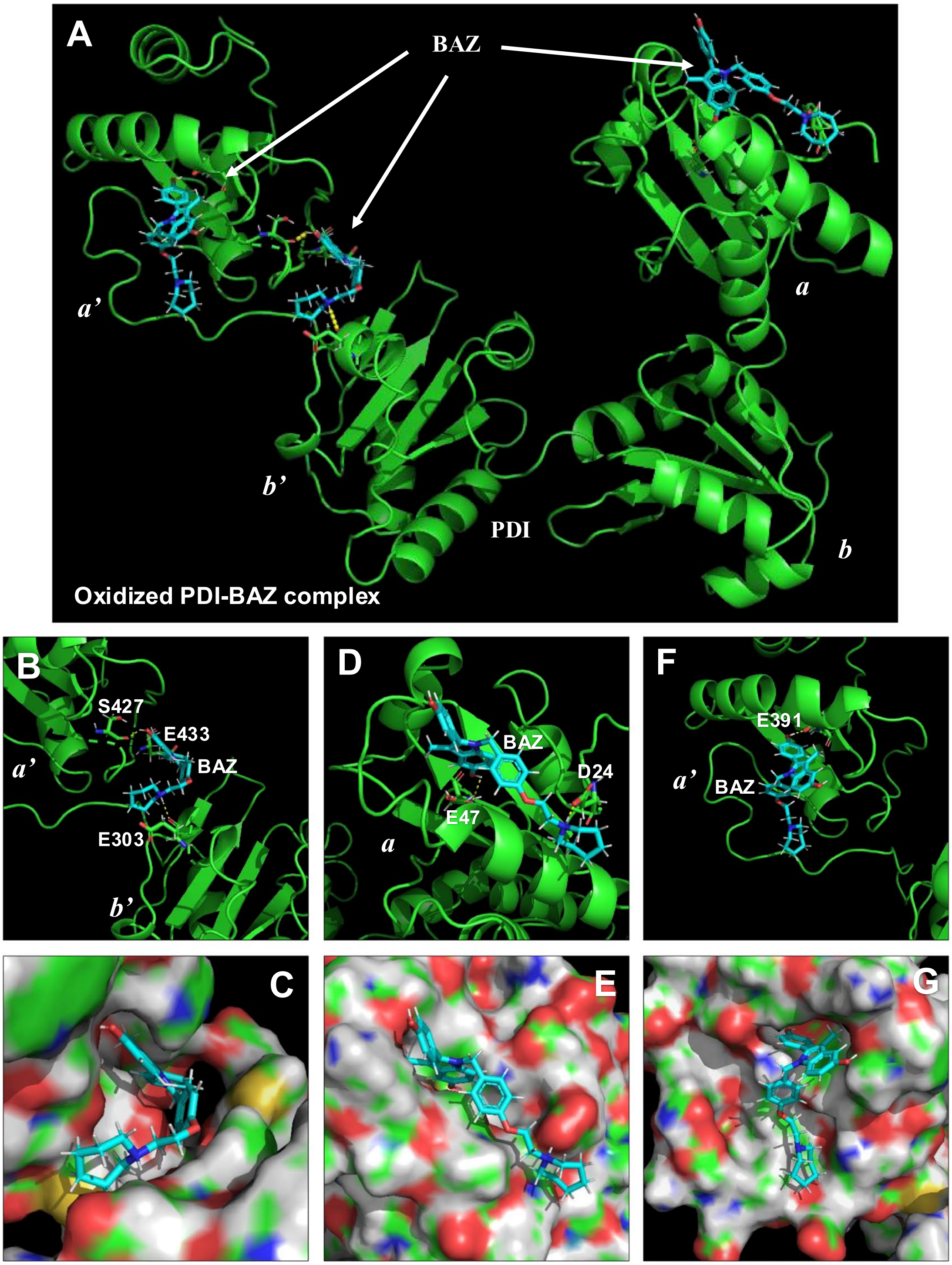

**Fig. 5** Predicted global structures of the oxidized PDI–BAZ complexes and the enlarged local structures of the binding pockets. **A**. Predicted global structures of the oxidized PDI–BAZ complexes. Three binding sites are identified for the binding interactions of BAZ with the oxidized PDI, which includes the binding site 1 between the ***a'*** and ***b'*** domains, the binding site 2 in the ***a*** domain (near the active site), and the binding site 3 in the ***a'*** domain (near the active site). **B**–**G**. Local enlarged structures of the binding pockets of the representative oxidized PDI–BAZ complexes. Three hydrogen bonds are found between BAZ and oxidized PDI at the binding site 1 in the representative docking pose #1 (**B**); two hydrogen bonds are formed at the binding site 2 in the representative docking pose #6 (**D**); and only one hydrogen bond is formed in the binding site 3 in the representative docking pose #10 (**F**). In these structures, PDI and BAZ are colored in green and cyan, respectively. Panels **C**, **E** and **G** are the surface features of PDI's binding pockets. The green regions are for carbon atoms, the blue regions for nitrogen atoms, the red regions for oxygen atoms, the white regions for hydrogen atoms, and the yellow regions for sulfur atoms, respectively

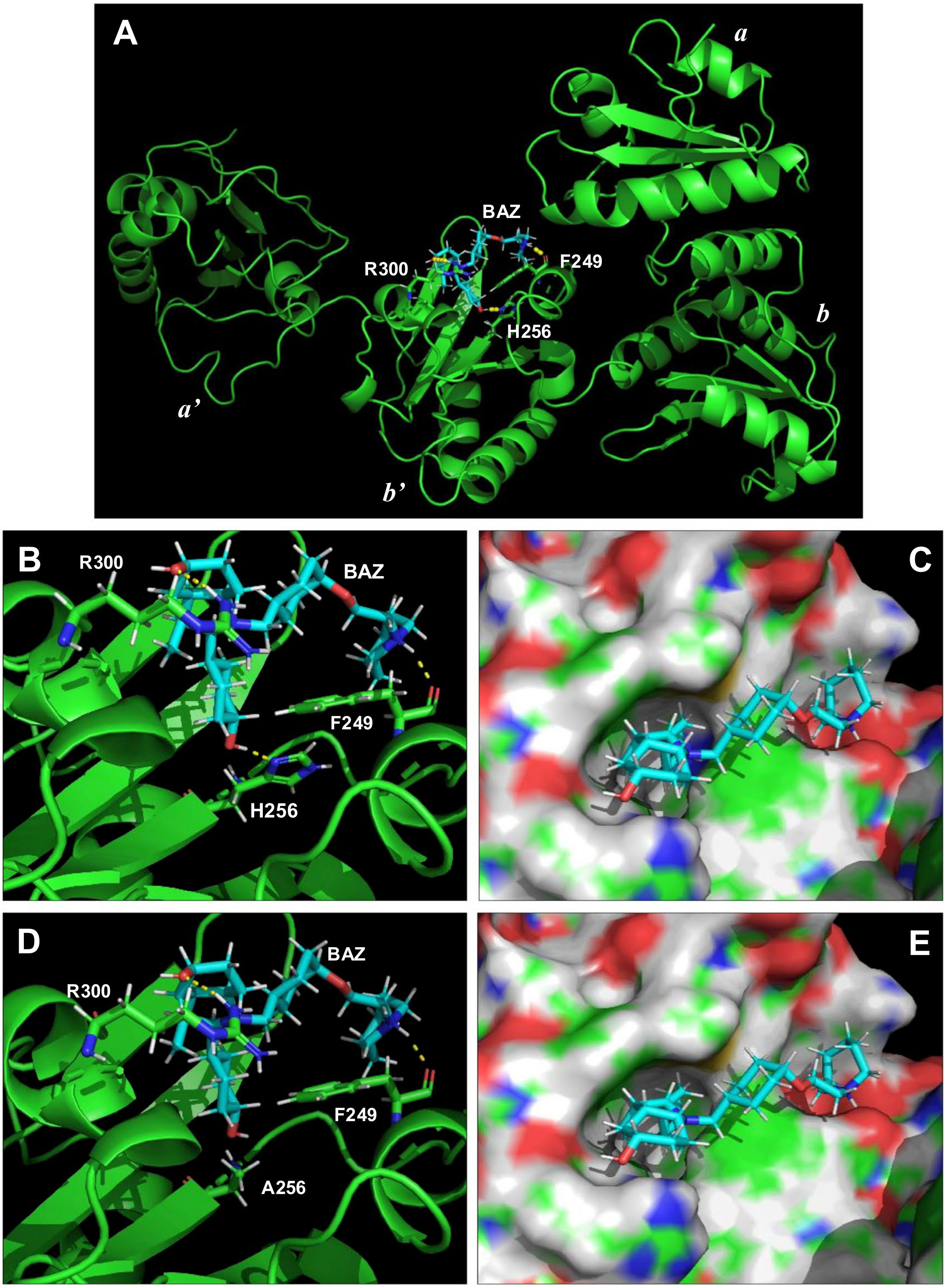

**Fig. 6** Predicted global structures of the wild-type and mutant PDI–BAZ complexes and the enlarged local structures of the binding pockets. **A**. Predicted global structure of the wild-type PDI-His256–BAZ complex (representative docking pose #1). Three hydrogen bonds are formed between the wild-type PDI-His256 and BAZ, and the involved residues (H256, F249 and R300) and BAZ are shown as sticks. PDI-His256 and BAZ are colored in green and cyan, respectively. **B**–**E**. Local structures of the binding pockets in the docking poses of the wild-type and the mutant PDI–BAZ complexes after MD simulation (**B**, **D**). Three hydrogen bonds are formed between BAZ and the wild-type PDI-His256 (**B**), but only two hydrogen bonds are formed between BAZ and the mutant PDI-Ala256 (**D**). In the local structure, the PDI and BAZ are colored in green and cyan, respectively. Panels **C** and **E** are the surface of the binding pockets of the wild-type and mutant PDI. The green regions are for carbon atoms, the blue regions for nitrogen atoms, the red regions for oxygen atoms, the white regions for hydrogen atoms, and the yellow regions for sulfur atoms, respectively

**Table 2** Basic information of the representative structures of the oxidized PDI–BAZ complexes

| No. | PDBcode_ChainID | X-Score (*Kcal/* mol) | PRODIGY-LIG (*Kcal/* mol) | $\Delta_{vina}RF_{20}$ | Number of hydrogen bonds between PDI and BAZ | Number of hydrogen bonds between PDI's H256 and BAZ | Binding site location |
|---|---|---|---|---|---|---|---|
| 1 | 4EL1_A | −8.79 | −9.21 | 5.43 | 3 | 0 | between ***a′*** and ***b′*** domains |
| 2 | 4EL1_A | −8.59 | −9.34 | 4.79 | 1 | 0 | between ***a′*** and ***b′*** domains |
| 3 | 4EL1_A | −8.4 | −9.11 | 3.3 | 1 | 0 | between ***a′*** and ***b′*** domains |
| 4 | 4EL1_A | −8.36 | −9.21 | 5.03 | 1 | 0 | between ***a′*** and ***b′*** domains |
| 5 | 4EL1_A | −8.4 | −9.14 | 5.21 | 1 | 0 | between ***a′*** and *b′* domains |
| 6 | 4EL1_A | −8.62 | −8.70 | 5.05 | 2 | 0 | in the ***a*** domain (near the active site) |
| 7 | 4EL1_A | −8.54 | −9.04 | 4.97 | 2 | 0 | in the ***a*** domain (near the active site) |
| 8 | 4EL1_A | −8.4 | −9.17 | 4.2 | 2 | 0 | in the ***a*** domain (near the active site) |
| 9 | 4EL1_A | −8.56 | −9.28 | 4.25 | 2 | 0 | in the ***a*** domain (near the active site) |
| 10 | 4EL1_A | −8.39 | −9.09 | 4.35 | 1 | 0 | in the ***a′*** domain (near the active site) |
| 11 | 4EL1_A | −8.39 | −9.09 | 4.32 | 1 | 0 | in the ***a′*** domain (near the active site) |
| 12 | 4EL1_A | −8.38 | −9.09 | 4.33 | 1 | 0 | in the ***a′*** domain (near the active site) |
| 13 | 4EL1_A | −8.37 | −9.1 | 4.14 | 1 | 0 | in the ***a′*** domain (near the active site) |
| 14 | 4EL1_A | −8.38 | −9.09 | 4.34 | 1 | 0 | in the ***a′*** domain (near the active site) |
| 15 | 4EL1_A | −8.38 | −9.09 | 4.35 | 1 | 0 | in the ***a′*** domain (near the active site) |

Note: Structure #1 is shown in Fig. 5B, C; structure #6 in Fig. 5D, E; and structure #10 in Fig. 5F, G

PDI–BAZ complex in all three MD simulation trajectories, the distance between BAZ and PDI-His256 remains very close in two of the MD simulation trajectories (Supplementary Fig. S26 A).

At the end of the 100-ns MD simulation (three trajectories), the hydrogen bond between BAZ and the wild-type PDI-His256 still exists in one complex (trajectory- 2; Fig. 7E), and this hydrogen bond exists for a cumulative duration of 43.1 ns (Supplementary Fig. S26B). In another PDI-His256–BAZ complex (Fig. 7D), BAZ moves slightly away from His256 at the end of MD simulation (trajectory- 1), and the hydrogen bond exists for a cumulative duration of 18.5 ns (Supplementary Fig. S26B). In the third complex shown in Fig. 7F, BAZ moves away from the wild-type PDI-His256 from the start, and no hydrogen bond is formed (trajectory- 3; Supplementary Fig. S26B). In contrast, for the three mutant PDI-Ala256–BAZ complexes, no hydrogen bond is found during the 100-ns MD simulation.

Lastly, it is of note that during MD simulations, the binding energies of the representative conformations of the wild-type PDI-His256–BAZ complexes are generally lower than those of the mutant PDI-Ala256–BAZ complexes, especially after 30-ns MD simulation (Supplementary Fig. S25B–S25D). These results are in line with the binding energy values for the seven representative PDI–BAZ complexes (docking structures) for both wild-type and mutant PDI proteins (Table 3). Together, these results illustrate the relative importance of His256 of the reduced PDI in its binding interaction with BAZ from both geometric and energy point of views.

### PDI mediates the protective effect of BAZ against chemically-induced ferroptosis

PDI knockdown. To provide experimental support for the hypothesis that BAZ rescues HT22 cells from chemically-induced ferroptosis through inhibition of PDI's catalytic activity, we selectively knocked down PDI expression in HT22 cells using PDI-specific siRNAs. The knockdown efficiency was confirmed by analyzing PDI protein levels (Fig. 8A). PDI knockdown significantly reduced erastin-induced ferroptosis in HT22 cells (Fig. 8B, C), and the protective effect of BAZ was partially diminished in PDI-knockdown cells (Fig. 8B, C). Similarly, PDI knockdown also decreased RSL3-induced ferroptosis (Fig. 8D, E), and the protective effect of BAZ against RSL3-induced

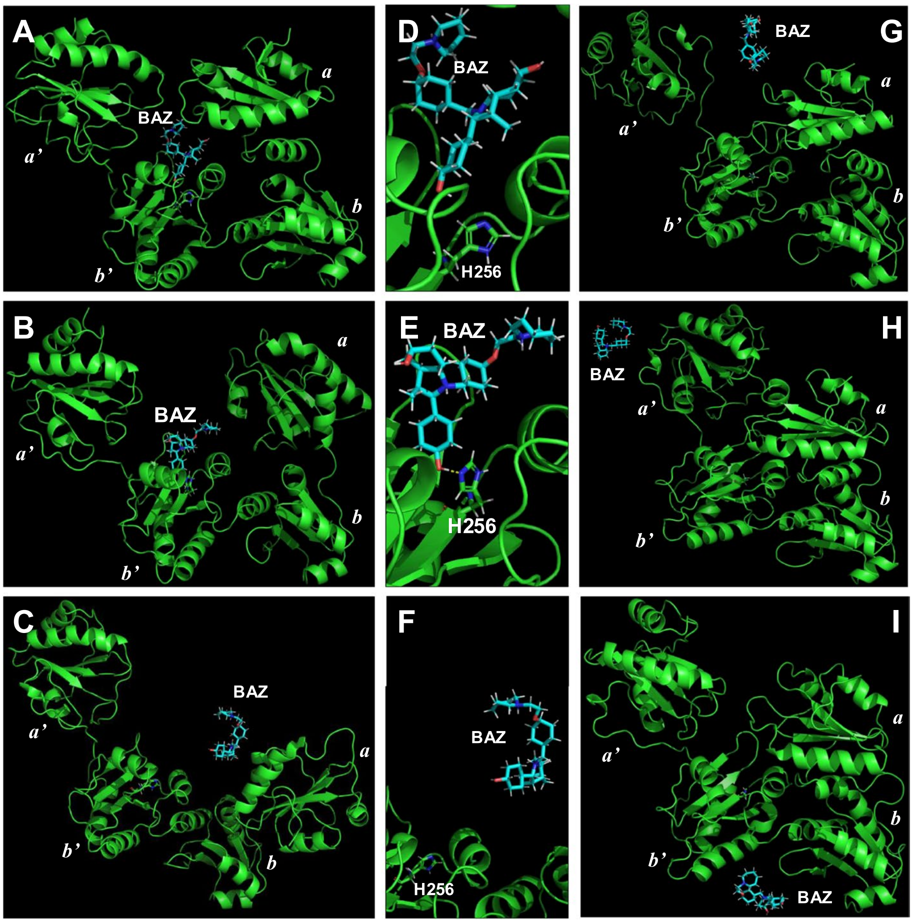

**Fig. 7** Conformations of the wild-type and mutant PDI–BAZ complexes after MD simulation. **A**–**C**. The last conformations the wild-type PDI-His256–BAZ complexes selected along the first (**A**), second (**B**) and third (**C**) MD trajectories. The BAZ is still bound to PDI-His256 in the first (**A**) and second (**B**) cases, but it is dissociated from PDI-His256 in the third case (**C**). **D**–**F**. The local structures of the binding pockets in the last conformations of the wild-type PDI-His256–BAZ complexes selected along the first (**D**), second (**E**) and third (**F**) MD trajectories. No hydrogen bond exists between BAZ and His256 in the first (**D**) and third (**F**) cases, and one hydrogen bond still exists between BAZ and His256 in the second case (**E**). **G**–**I**. The last conformation of the mutant PDI-Ala256–BAZ complex along the first (**G**), second (**H**) and third (**I**) MD trajectories. Note that BAZ is dissociated from the mutant PDI-Ala256 in all three cases

ferroptosis was also diminished by PDI knockdown (Fig. 8D, E). Here, it is worth noting that PDI knockdown exhibited a relatively modest protection against erastin/RSL3-induced ferroptosis, along with a partial attenuation of BAZ's cytoprotective effect. The modest efficacy of PDI knockdown may be due to the significant cytotoxicity associated with PDI knockdown *per se*, which masks its cytoprotective effect.

### *NOS dimerization and upregulation*

Next, we sought to determine whether BAZ can effectively inhibit erastin/RSL3-induced NOS dimerization and NO accumulation in HT22 cells through inhibition of PDI. Treatment of HT22 cells with BAZ abrogated erastin-induced increase in iNOS and nNOS dimerization as well as their total protein levels (Fig. 8F). In comparison, the PDI protein levels were not significantly altered by joint treatment with BAZ (Fig. 8H).

Similarly, joint treatment of HT22 cells with BAZ also abrogated RSL3-induced increase in iNOS and nNOS dimerization and total protein levels (Fig. 8G). PDI protein levels were not significantly affected by the joint treatment (Fig. 8I).

### BAZ protects against kainic acid-induced memory deficit and hippocampal neuronal injury in mice

To determine whether BAZ has neuroprotective effects *in vivo*, we used the kainic acid-induced neuronal damage in the hippocampal regions of mice as an *in vivo* model. The classical Y-maze test was used

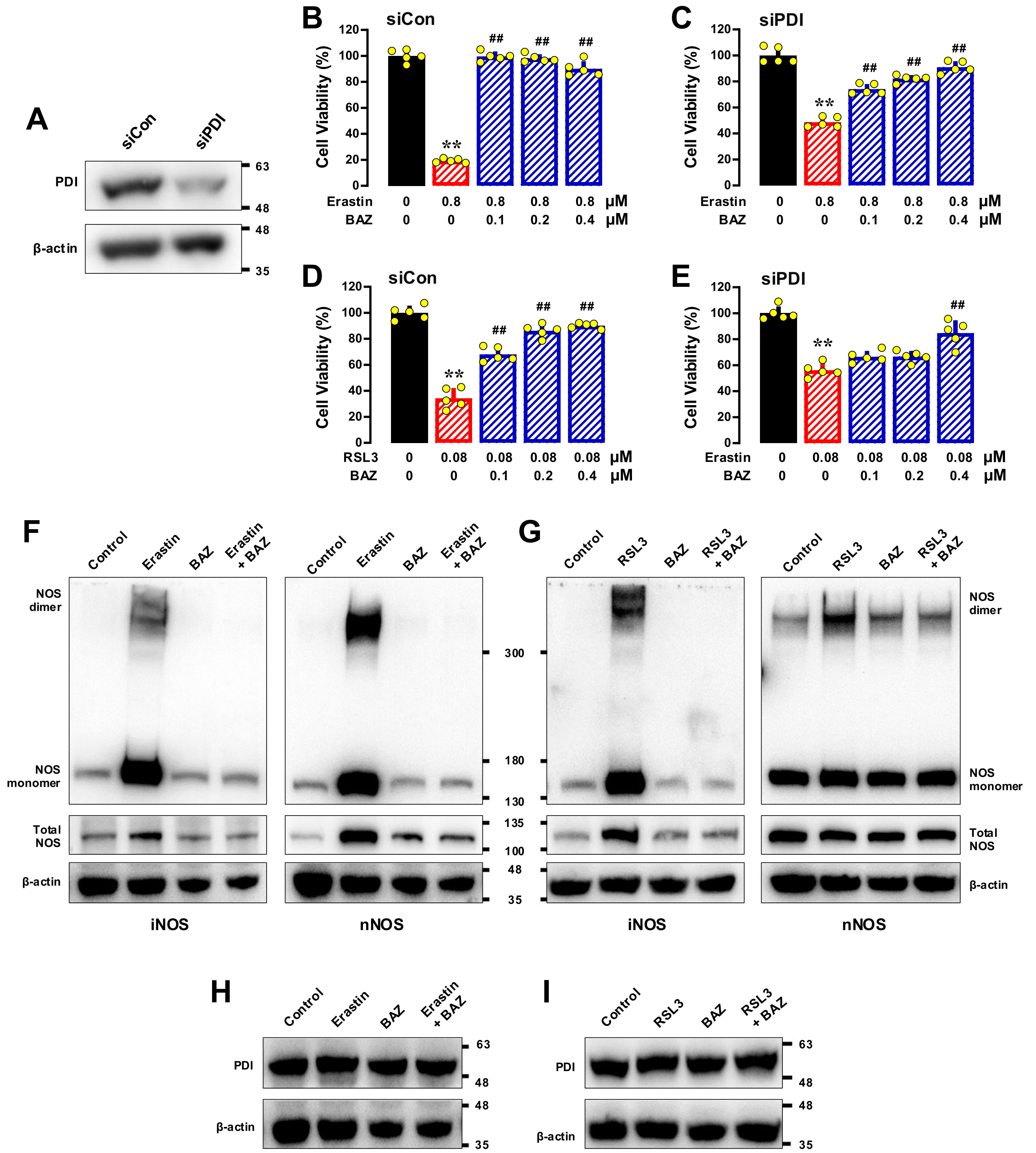

**Fig. 8** BAZ protects against ferroptotic cell death in HT22 cells by inhibiting PDI function. **A**–**E**. Effect of PDI knockdown on erastin/RSL3-induced ferroptosis and on cytoprotection by BAZ. Cells were transfected with control siRNAs (siCon) or PDI-specific siRNAs (siPDI) for 24 h, and then they were treated with 0.8 μM erastin ± BAZ (**B**, **C**) or 0.08 μM RSL3 ± BAZ (**D**, **E**) for 24 h. Cell viability was determined by MTT assay ($n = 5$). The efficiency of PDI knockdown was confirmed by Western blot analysis of cellular PDI protein levels (**A**). Quantitative data in **A**–**D** are presented as mean ± S.D. (** or $^{\#\#}$ $P < 0.01$). **F**. Abrogation by BAZ of erastin-induced increase in iNOS and nNOS dimerization and upregulation. Cells were treated with 0.8 μM erastin ± 1 μM BAZ for 8 h, and then levels of total cellular iNOS and nNOS proteins and their dimers and monomers were determined by Western blotting (left penals for iNOS; right penals for nNOS). **G**. Abrogation by BAZ of RSL3-induced increase in iNOS and nNOS dimerization and upregulation. Cells were treated with 0.08 μM RSL3 ± 1 μM BAZ for 8 h, and then levels of total cellular iNOS and nNOS proteins and their dimers and monomers were determined by Western blotting (left penals for iNOS; right penals for nNOS). **H, I.** Levels of cellular PDI protein (Western blotting) following 8-h treatment with 0.8 μM erastin ± 1 μM BAZ (**H**) or 0.08 μM RSL3 ± 1 μM BAZ (**I**). For Western blotting, the experiments were repeated three times to confirm the observations; the data from a representative assay is shown here

to evaluate the working memory in these animals. The basic assumption of the classical Y-maze test is that when an animal reaches the center of the maze and is faced with the choice of two new arms, it would tend to explore the arm which has not been explored right before (Fig. 9B). Based on this assumption, the theoretical alternation rate is thought to be 100% for a normal healthy mouse. However, we found that under real experimental conditions, the real alternation rate of the control mice (receiving saline vehicle injections only) was only 71.0 ± 2.6% (Fig. 9C), and this value is largely in agreement with some of the reported values (about 70%) in earlier studies [83, 85, 88]. The alternation rate in kainic acid-injected mice was found to be around 50%. This value is as expected since the kainic acid-injected mice would have damaged the hippocampus and impaired the working memory of these animals. As such, the kainic acid-treated animals could not remember as well which arm it had already explored right before, and consequently, it would be more likely to make a random choice when faced with two options. The alternation rates of kainic acid-injected mice jointly treated with 3 and 5 mg/kg BAZ were 65.5 ± 1.8% ($P < 0.01$) and 64.1 ± 1.7% ($P < 0.01$), respectively, which were significantly higher than the corresponding rates in animals injected with kainic acid alone. However, animals jointly receiving 1.5 mg/kg BAZ (the lowest dose tested) only had a very small improvement compared with kainic acid-injected animals (51.0 ± 3.2% *vs* 55.5 ± 2.4%; $P = 0.026\%$) (Fig. 9C).

In the present study, a new Y-maze-based behavioral test was designed which enabled us to conduct additional assessment of the protective effect of BAZ on the learning and memory functions using the same kainic acid-injected mice. The procedures of this new behavioral test is described in detail in the methods section, and the data are summarized in Fig. 9D, E. As shown in Fig. 9B, the food was placed in one arm of the Y-maze and the mouse was placed at the end of another arm (*i.e.*, the starting arm). Then the animal was allowed to freely explore the maze and would find the food and eat it. It was observed that nearly all the mice in the control group could correctly remember which arm contained food starting from the 7th to 9th trials and onward; in comparison, the kainic acid-injected animals took significantly more trials to correctly remember which arm contained food. Compared to the animals injected with kainic acid alone, those animals jointly treated with 3 mg/kg BAZ and kainic acid had a markedly improved memory, with close to 80% correctness between 7th–9th trials and > 80% correctness thereafter (Fig. 9D).

For comparison, the overall time required for each animal to find the food and start eating it was also recorded in this behavioral test (Fig. 9E). It was observed that with increased number of trials, all mice in different experimental groups progressively improved their time, and eventually reached a similar plateau. This observation indicates that the animals in all treatment groups can gradually learn to perform this relatively simple task (*i.e.*, remembering the correct arm where the food is). However, in the first five trials, the differences among the four groups of animals were quite obvious, and there was a clear difference between the control group and kainic acid-injected group. The animals jointly treated with kainic acid + 1.5 or 3 mg/kg BAZ took significantly less time than the animals injected with kainic acid alone, indicating that BAZ effectively improves the memory function of kainic acid-treated mice (Fig. 9E).

In this study, histological analysis of the representative hippocampal CA3 region of mice at 6 d post kainic acid injection was analyzed to evaluate the neuroprotective effects of 3 mg/kg BAZ *in vivo*. Kainic acid-injected animals showed a drastic neuronal loss in the hippocampus, but joint treatment with 3 mg/kg BAZ for 7 d afforded almost complete neuroprotection in this brain region. The extent of neurodegeneration in the CA3 region was assessed using different methods (H/E, Fluoro-Jade B staining, and TUNEL assay) (Fig. 10A–C). In H/E staining, kainic acid injection caused a strong loss of neuronal nuclei in the CA3 region, while this region in animals jointly treated with 3 mg/kg BAZ was strongly protected against kainic acid-induced neuronal death, almost making it not too different morphologically from the vehicle-treated control animals (Fig. 10A). This observation indicates that BAZ has a strong protective effect against kainic acid-induced oxidative neuronal loss *in vivo*. The observation made with the H/E-stained brain histology slides was also consistent with the slides analyzed with the Fluoro-Jade B staining. Fluoro-Jade B is an anionic fluorochrome capable of selectively staining

(See figure on next page.)

**Fig. 9** BAZ attenuates kainic acid (KA)-induced learning and memory impairment in a mouse model *in vivo*. **A**, **B**. The time scheme of the animal experiments (**A**) and the illustration of the Y-maze tests used in this study (**B**). **C**. Working memory of the animals in different treatment groups based on the alternation rates in the classical Y-maze test, conducted at 6 days after kainic acid (KA) treatment. **D**. Learning ability of the animals in different treatment groups assessed according to the correct rates (% of maximum) in finding the food in different trial cycles. Note that the data from every three consecutive trials (except the last two trials) were used to calculate the mean value for one cycle. **E**. Learning ability of the animals in different treatment groups assessed according to the time (in seconds) taken to find the food in the first ten trials. All quantitative data are presented as mean ± S.D. ($n = 6–7$; * or $^{\#}$ $P < 0.05$; ** or $^{\#\#}$ $P < 0.01$)

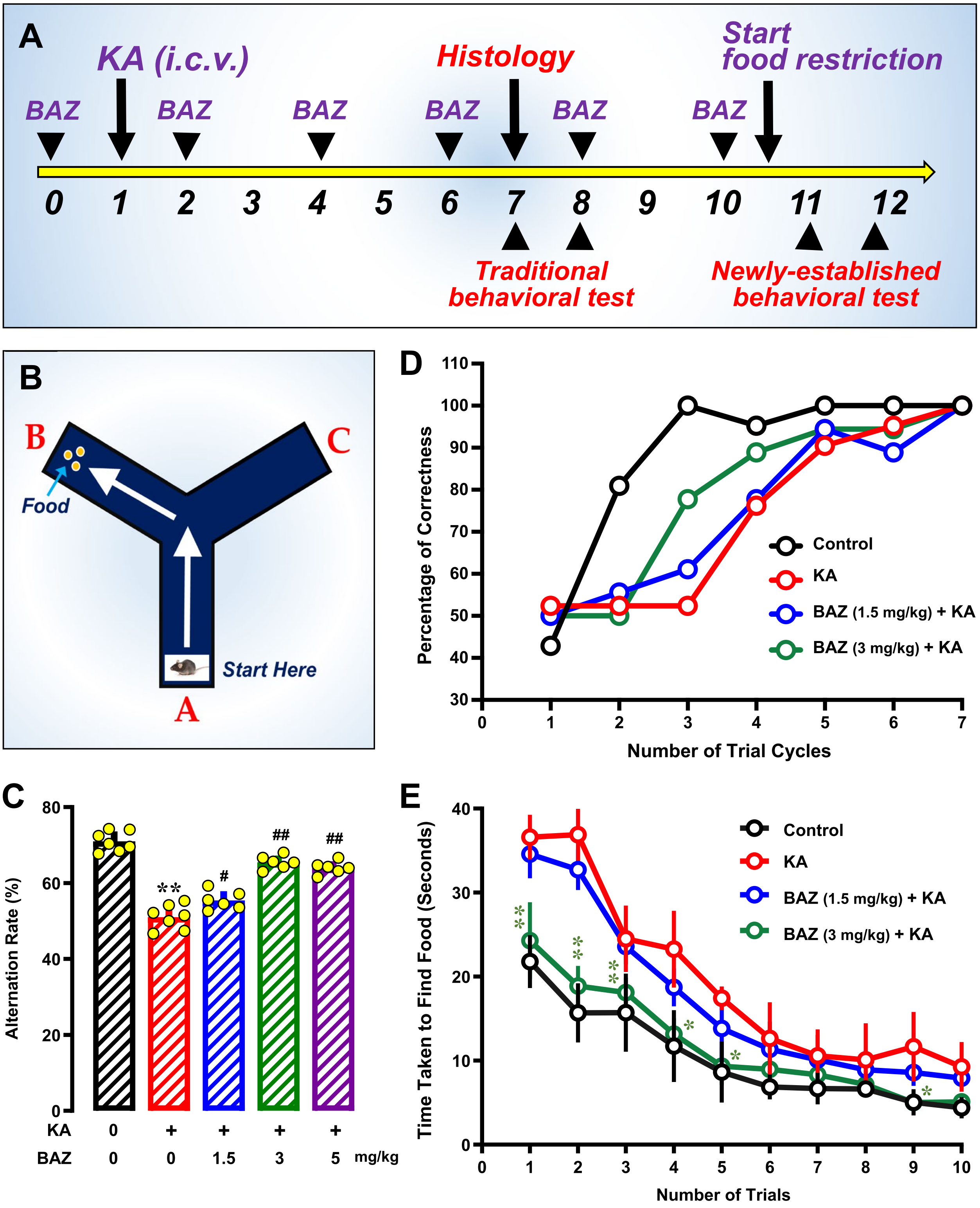

**Fig. 9** (See legend on previous page.)

degenerating neurons in brain slices [89]. In the CA3 region in kainic acid-injected animals, a majority of neurons were strongly stained with Fluoro-Jade B (124.3 ± 17.5), whereas animals jointly treated with 3 mg/kg BAZ and kainic acid had a markedly reduced number of neurons in this region stained with Fluoro-Jade B (32.3 ± 8.7, $P < 0.01$) (Fig. 10B).

TUNEL assay selectively detects damaged cells that undergo oxidative DNA degradation, and is considered as a marker of apoptosis. Interestingly, recent studies reported that TUNEL activity is markedly increased during the induction of ferroptosis both in animal models [90–93] and also in cell culture after challenged with prototypical ferroptosis inducers [94, 95]. In this study, we also found that BAZ elicits a strong reduction in TUNEL staining of CA3 hippocampal neurons (Fig. 10C), which is in line with its strong neuroprotective actions *in vitro* and *in vivo*. Similarly, in our earlier studies, 4-OH-$E_1$ (another PDI inhibitor) also strongly reduced TUNEL staining in hippocampal neurons of kainic acid-treated animals [82].

These results reveal that kainic acid-induced memory impairments in an animal model can be partially rescued by BAZ administration. Histochemical analyses confirm that BAZ can protect mouse hippocampal neurons from kainic acid-induced neuronal injury.

## Discussion

### BAZ has a strong neuroprotective action *in vitro* and *in vivo*

In this study, we demonstrate that BAZ has a strong protective action against chemically-induced oxidative cell death in hippocampal neurons both *in vitro* and *in vivo*. Using the HT22 mouse hippocampal neurons as an *in vitro* model, we show that treatment of these cells with erastin or RSL3 can readily induce oxidative cell death, and joint treatment of these cells with very low concentrations of BAZ (at 62.5−1000 nM) can strongly rescue them from erastin/RSL3-induced cytotoxicity in a concentration-dependent manner. The protective efficacy of BAZ is very high, and 100% protection against erastin- and RSL3-induced ferroptosis is observed when BAZ is present at 500 nM and 250 nM, respectively. It appears that BAZ has a higher potency in rescuing the cytotoxicity of RSL3 than that of erastin.

We also show that BAZ can effectively protect against kainic acid-induced memory deficit and hippocampal neuronal injury in an *in vivo* model. Administration of 1.5, 3 and 5 mg/kg BAZ improves the memory and learning performance of kainic acid-injected mice in a dose-dependent manner. The effect of BAZ on improving mouse learning and memory functions observed in this study is in agreement with an earlier report on its neuroprotective activity in another animal model [45]. Histochemical analysis of the representative hippocampal CA3 brain region of mice 6 d post kainic acid injection shows a drastic neuronal loss, but joint treatment with BAZ (at 3 mg/kg) for 7 d affords almost complete protection in this brain region.

This study reveals that BAZ has a super-high efficacy in reducing the levels of all cellular ROS, including cytosolic ROS, lipid-ROS and mitochondrial ROS. Since BAZ at concentrations well below 1 μM already exhibits a completion protection against chemically-induced cytotoxicity along with a near-complete abrogation of cellular ROS, lipid-ROS and mitochondrial ROS accumulation, it is almost certain that BAZ does not exert this function solely by serving as a chemical scavenger for all forms of cellular ROS. The reason is rather simple as the total levels of all cellular ROS, lipid-ROS and mitochondrial ROS would be much higher than the effective concentrations of BAZ. Therefore, it is speculated that there must be a highly specific mechanism which mediates the strong antioxidant and neuroprotective actions of BAZ.

It has been previously suggested that BAZ's neuroprotective actions may involve the activation of estrogen receptors and/or GRP30 [46]. However, the results of this study clearly show that the ER binding affinity of BAZ does not contribute meaningfully to its neuroprotective actions. This suggestion is supported by our observations that the same protective effect of BAZ was also observed in the estrogen receptor-negative MDA-MB- 231 human breast cancer cells [53] after they were challenged with erastin or RSL3 (Supplementary Fig. S1 A, S10 A). In addition, BAZ exhibits a similar protective effect against

(See figure on next page.)

**Fig. 10** BAZ attenuates kainic acid (KA)-induced neurodegeneration in selected mouse hippocampal regions *in vivo*. **A**. Representative data for the histopathological analysis of the damaged hippocampal region. The upper two panels are the H/E staining of the hippocampal region (scale bar = 2 mm) and the enlarged CA3 region (scale bar = 200 μm), respectively. The middle two panels are the Fluoro-Jade B staining of the hippocampal region (scale bar = 2 mm) and the enlarged CA3 region (scale bar = 200 μm), respectively. The bottom panel is the TUNEL staining of cells in the CA3 region (scale bar = 60 μm). **B**. Quantitative data for the number of degenerating neurons in control and kainic acid (KA)-treated mice ($n = 3$). **C**. Relative intensity of TUNEL staining in CA3 neuronal cells in control and kainic acid (KA)-treated mice ($n = 3$). All quantitative data are presented as mean ± S.D. (* or $^{\#}$ $P < 0.05$; ** or $^{\#\#}$ $P < 0.01$)

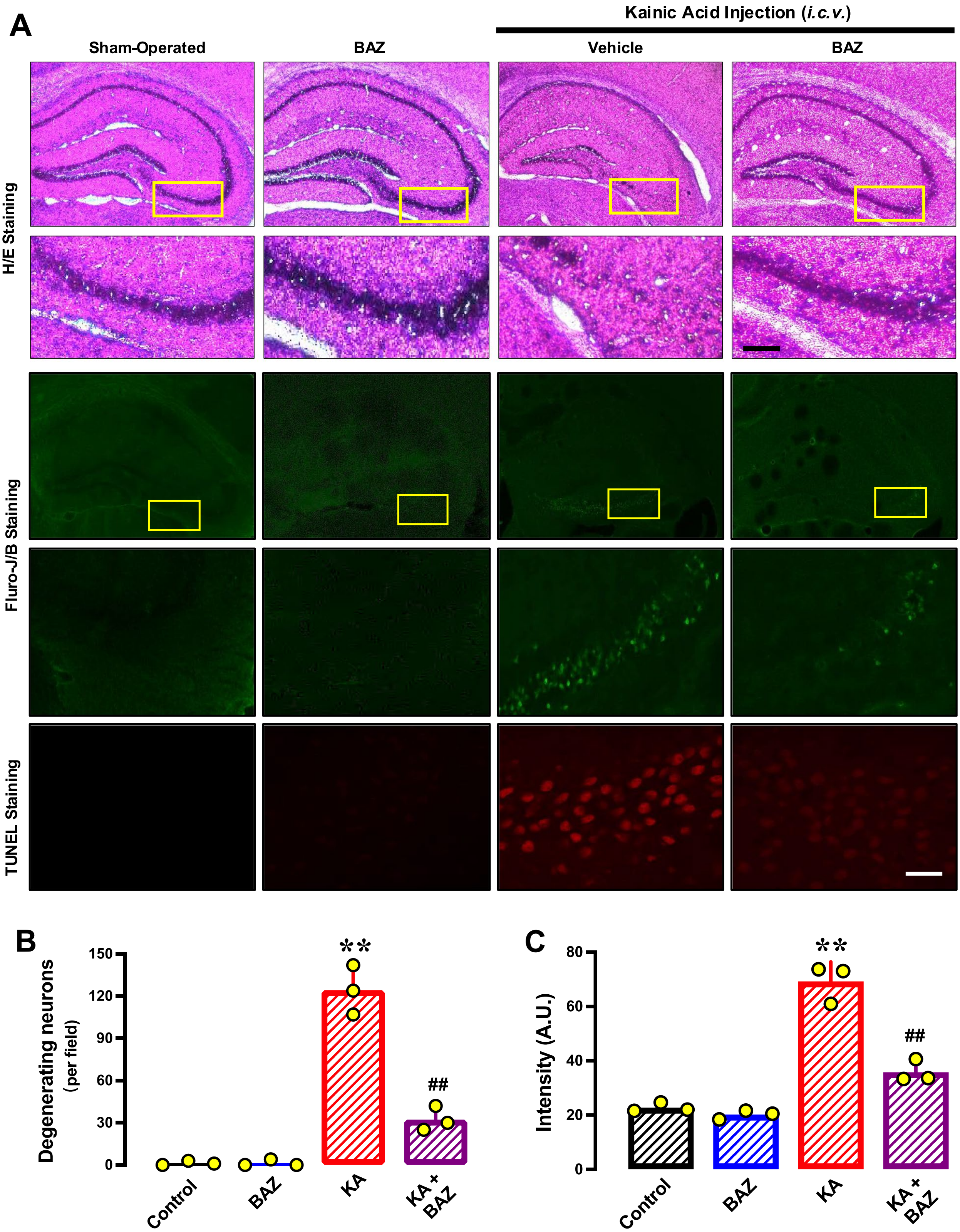

**Fig. 10** (See legend on previous page.)

chemically-induced cell death in a few other cell lines tested in this study.

### Role of PDI in mediating BAZ's neuroprotection

Recently, we have gathered considerable evidence to show that PDI is a mediator of chemically-induced ferroptosis. First, we found that PDI inhibitors can effectively rescue cells from chemically-induced ferroptosis. For instance, cystamine, a known PDI inhibitor [96], can strongly rescue cells from against erastin/RSL3-induced ferroptosis [15, 32, 33, 97], and the cytoprotection is associated with reduced NOS dimerization and reduced NO and ROS/lipid-ROS accumulation. Additionally, we have recently shown that cystamine can prevent acetaminophen-induced hepatocyte injury *in vivo* [15]. Mechanistically, the cytoprotective action of cystamine is purely due to its ability to covalently modify the free –SH group(s) in PDI's catalytic sites, resulting in PDI inactivation and reduced NOS dimerization. Similarly, 4-hydroxyestrone, another inhibitor of PDI, also strongly rescues from erastin/RSL3-induced ferroptosis in culture [98, 99]. Second, like PDI inhibitors, we have recently shown that genetic manipulations of PDI expression can reduce the cytotoxicity of erastin and RSL3 *in vitro* [32, 33, 98] and acetaminophen-induced liver injury *in vivo* [15]. The effect of PDI knockdown on erastin/RSL3-induced cell death is also confirmed in this study. Additionally, PDI knockdown partially alleviates the protective effect of BAZ against erastin/RSL3-induced neurotoxicity in HT22 cells.

The recent advances in our understanding of PDI's role in oxidative ferroptosis have prompted the speculation that BAZ may exert its neuroprotective action through inhibiting PDI's catalytic activity, which then reduces NOS dimerization, and ultimately, prevents neuronal ferroptosis (as depicted in Fig. 11). As summarized below, several lines of evidence are obtained in this study which jointly offers support for this hypothesis:

First, surface plasmon resonance assay shows that BAZ can bind to purified PDI protein with a high binding affinity (apparent $K_d$ of 3.3–3.6 nM). In addition, BAZ can bind to PDI in live HT22 cells and increases PDI protein thermos-stability in a concentration-dependent manner.

Second, PDI has both oxidase (*i.e.*, the linkage of two free thiol groups in protein substrates to form a disulfide bond) and reductase activities (*i.e.*, the reduction of a disulfide bond in protein substrates to two free thiol groups). Our enzyme assays reveal that BAZ can inhibit both oxidase and reductase activities of the wild-type PDI. Since PDI's oxidase activity mediates the dimerization of iNOS and nNOS, an inhibition of this activity by BAZ will result in reduced NOS dimerization in neuronal cells challenged with erastin/RSL3, which then reduces the accumulation of cellular NO and ROS (including lipid-ROS and mitochondrial ROS) and prevents oxidative cell death.

Moreover, an inhibition of PDI's reductase activity by BAZ may also contribute to the observed cytoprotective actions of BAZ via two potential mechanisms. First, the binding of BAZ to the reduced PDI protein may decrease its chances for oxidation (*i.e.*, catalytic activation of PDI) by other cellular components. Second, if we assume that the reduced PDI can catalyze the conversion of NOS dimers back to their monomers (this is presently unclear), then BAZ's binding to the reduced PDI would reduce its ability to bind the dimeric NOS substrates for reduction.

Third, computational modeling reveals that BAZ can bind tightly inside a rather deep pocket between ***b'*** and ***b*** domains of the reduced PDI, forming a hydrogen bond with its His256. The important role of BAZ's interaction with His256 is also confirmed by MD simulation analysis. Additionally, it should be noted that there are multiple Phe residues in the binding pocket which may form hydrophobic interactions with the highly-lipophilic BAZ molecule, partly contributing to its binding interactions with PDI.

The importance of PDI's His256 in the formation of PDI–BAZ complex is in agreement with the enzyme activity results showing that BAZ cannot inhibit the reductase activity of the mutant PDI-Ala256. It is known that when the reduced PDI catalyzes disulfide bond reduction, the substrate is one protein molecule (such as the dimeric NOS protein). Earlier studies have revealed that PDI's His256 is involved in the binding of certain protein substrates [61, 100]. As such, when BAZ is tightly bound to PDI through His256, it may competitively inhibit the further entry of the protein substrate due to steric interference. However, for the mutant PDI-Ala256, BAZ does not bind to its Ala256 and it does not inhibit PDI's reductase activity. Since we find that the mutant PDI-Ala256 still retains its maximal reductase activity with a reduced catalytic velocity, this clearly indicates that the protein substrate can still bind, with a reduced affinity, to PDI in the absence of His256.

For the oxidized PDI, computational modeling suggests that BAZ may have three binding sites (Fig. 5A, Table 2): one located between the *a'* and *b'* domains, one in the *a* domain near an active site, and another one in the *a'* domain also near an active site. Modeling results from this study as well as from our recent study [66] both reveal that PDI can undergo spontaneous

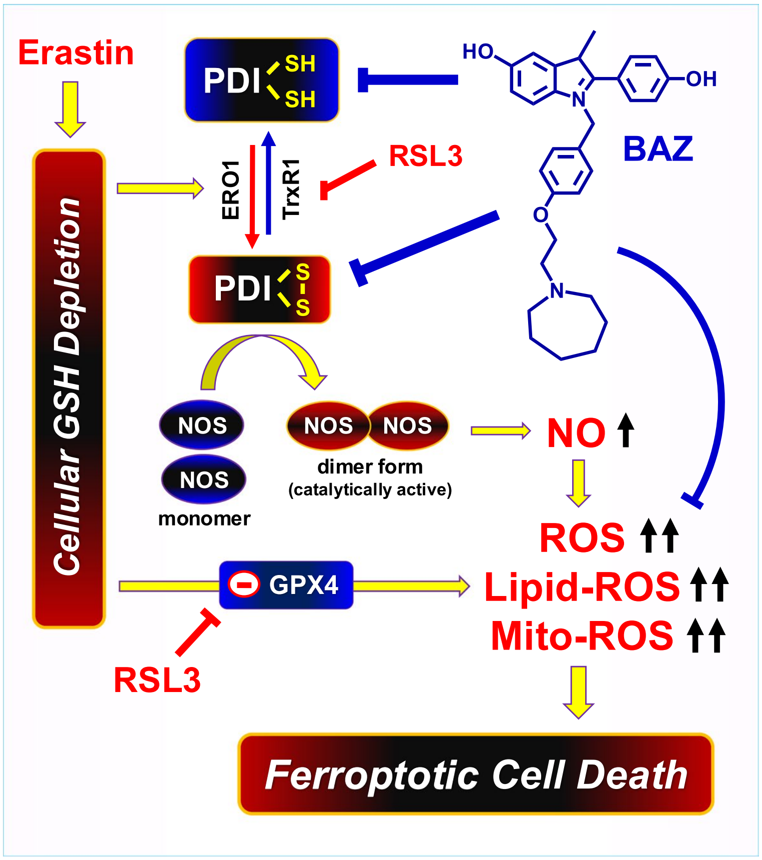

**Fig. 11** Schematic depiction explaining the mechanism by which PDI mediates the neuroprotective action of BAZ against chemically-induced ferroptosis. For detailed explanation, please refer to the Discussion section

**Table 3** Predicted binding affinities based on the seven representative predicted structures of wild-type reduced PDI–BAZ complexes or the Ala256 mutant reduced PDI–BAZ complexes

| PDI–BAZ complex # | Number of hydrogen bonds between BAZ and PDI proteins | | Number of hydrogen bond between BAZ and His256 | | *X*-Score (*K*cal/mol) | | PRODIDY-LIG (*K*cal/mol) | | $\Delta_{\mathrm{vina}}\mathrm{RF}_{20}$ | |
|---|---|---|---|---|---|---|---|---|---|---|
| | PDI-His256 | PDI-Ala256 | PDI-His256 | PDI-Ala256 | PDI-His256 | PDI-Ala256 | PDI-His256 | PDI-Ala256 | PDI-His256 | PDI-Ala256 |
| 1 | 3 | 2 | 1 | 0 | − 9.44 | − 9.22 | − 8.93 | − 8.69 | 6.51 | 6.28 |
| 2 | 2 | 1 | 1 | 0 | − 9.57 | − 9.41 | − 9.11 | − 8.84 | 5.74 | 5.52 |
| 3 | 2 | 1 | 1 | 0 | − 9.34 | − 9.15 | − 9.24 | − 9.04 | 5.54 | 5.35 |
| 4 | 2 | 1 | 1 | 0 | − 9.63 | − 9.38 | − 8.91 | − 8.66 | 6.12 | 5.85 |
| 5 | 3 | 2 | 1 | 0 | − 9.49 | − 9.28 | − 8.96 | − 8.72 | 5.85 | 5.63 |
| 6 | 1 | 0 | 1 | 0 | − 9.42 | − 9.25 | − 9.01 | − 8.75 | 5.82 | 5.6 |
| 7 | 1 | 0 | 1 | 0 | − 9.26 | − 9.14 | − 8.96 | − 8.75 | 6.04 | 5.84 |

interconversions between its closed states and open states, regardless of PDI's oxidation/reduction states. For the oxidized PDI to catalyze disulfide bond formation, it needs to simultaneously bind two protein substrates (one binds to the catalytic site in *a'* domain, and the other one binds to the catalytic site in the *a* domain; depicted in Supplementary Fig. S27 A, S27B). As such, PDI needs to be in its open states for this function. Once the substrate binding finishes, then PDI needs to adopt the closed states so that it can catalyze the formation of the disulfide bond (depicted in Supplementary Fig. S27 C). Because of these required conformational changes, the binding of

BAZ at the hinge regions between PDI's *a'* and *b'* domains is expected to affect the agile transition between PDI's different conformations, thereby inhibiting its oxidase activity (Supplementary Fig. S27D).

As for the binding of BAZ to the two other binding sites of an oxidized PDI near the catalytic sites in the ***a'*** and ***a*** domains, each scenario will directly affect the further binding of substrate proteins to these active sites, and thus will directly inhibit the catalytic activity for disulfide bound formation. Lastly, computational modeling analysis also predicts that BAZ does not interact with His256 of an oxidized PDI, and this prediction fully agrees with the enzyme activity results.

Fourth, the finding that BAZ can bind tightly to PDI and effectively inhibit its catalytic activity *in vitro* is also corroborated by the biochemical changes observed in erastin-treated cells. Specifically, it is observed that treatment of HT22 cells with erastin alone results in PDI-mediated iNOS and nNOS activation (*i.e.*, formation of NOS dimers) along with cellular NO accumulation, and joint treatment of cells with BAZ abrogates erastin-induced iNOS and nNOS dimerization and NO accumulation. In addition, BAZ suppresses erastin-induced upregulation of NOS proteins, which also contributes to erastin-induced cytotoxicity.

Here it should be noted that in HT22 cells, we find that erastin-induced $ONOO^-$ accumulation is abrogated by joint treatment with either BAZ or urea. However, while BAZ strongly protects against erastin-induced cell death, urea does not exhibit a meaningful protection. Urea reduces $ONOO^-$ levels in erastin-treated cells through its direct $ONOO^-$-scavenging activity, but BAZ reduces $ONOO^-$ level through its inhibition of PDI, which then reduces the formation of the catalytically-active NOS dimers and NO, and ultimately, reduces the conversion of NO to $ONOO^-$ as well as its accumulation. Since BAZ elicits a strong cytoprotection but urea does not have this protective effect, it is apparent that $ONOO^-$ is not the main culprit that mediates chemically-induced ferroptosis. This observation offers additional support for the notion that NO (but not $ONOO^-$) is an important upstream element that drives chemically-induced ferroptosis.

Fifth, based on the observations made in this study, it is evident that PDI is also similarly involved in mediating RSL3-induced ferroptosis in HT22 neuronal cells, and inhibition of PDI's function by BAZ contributes to its protection against RSL3-induced cell death. RSL3 is a prototypical ferroptosis inducer, and it has long been thought that its ferroptosis-inducing activity is primarily due to its inhibition of GPX4 [101]. However, recent studies have shown that RSL3 can also strongly inhibit the enzymatic activity of TrxR1 [33, 35]. Theoretically, inhibition of TrxR1 by RSL3 would shift the pool of cellular PDI proteins (a member of the thioredoxin superfamily) toward the catalytically-active oxidized state, thus favoring NOS dimerization. Recently, we have shown that in addition to inhibition of GPX4, RSL3, through its ability to inhibit TrxR1 enzymatic activity [33, 35], can facilitate PDI oxidation and promote RSL3-induced ferroptosis by facilitating NOS dimerization, followed by cellular NO, ROS and lipid-ROS accumulation, and ultimately ferroptotic cell death [33]. This novel mechanism of RSL3-induced ferroptosis also provides a good explanation for the strong neuroprotective effect of BAZ against RSL3-induced ferroptosis, which is supported by experimental observations made in this study. For instance, we find that there is a time-dependent increase in total NOS protein levels in HT22 cells treated with 0.08 μM RSL3, and joint treatment of HT22 cells with BAZ abrogates RSL3-induced increase in total NOS protein and its dimer levels.

It is observed in this study that BAZ exhibits a markedly stronger protection against RSL3-induced ferroptotic cell death compared to erastin-induced cell death. It is possible that the direct antioxidant activity of BAZ against lipid-ROS may partially contribute to its cytoprotective effect, in addition to PDI inhibition. This possibility is in line with the fact that BAZ is a highly hydrophobic compound, and its antioxidant activity would be more readily manifested in protection against cellular lipid peroxides which are induced by treatment with RSL3. This suggestion is also consistent with an earlier report that BAZ is an inhibitor of ferroptosis with free radical-trapping activity [102].

## Conclusions, limitations and future directions

As summarized in Fig. 11, the results of our study demonstrates that BAZ, a third generation SERM, exerts its strong protective effect against chemically-induced ferroptosis in hippocampal neurons both *in vitro* and *in vivo* through inhibition of PDI-mediated activation of NOS/NO in cells challenged with erastin or RSL3, which subsequently results in reductions in cellular ROS and lipid-ROS levels, and ultimately ferroptotic cell death. In addition, the direct antioxidant activity of BAZ may also partially contribute to its protective effect against chemically-induced ferroptosis. These findings reveal a novel mechanism of estrogen receptor-independent neuroprotection by BAZ.

The present study, however, also presents limitations. While the immortalized HT22 hippocampal neurons are tested as an *in-vitro* model in this study, it is not known whether a similar ferroptosis-rescuing effect of BAZ can also be manifested in other neuronal models. Another limitation is related to the animal model and functional tests used in this study. Although BAZ is effective in two Y-maze-based memory tests, it is not known how well these simple learning/memory tests correlate with the cognitive impairments in human neurodegenerative conditions (*e.g.*, Alzheimer's disease).

Lastly, while BAZ is presently approved for use as a preventive agent for postmenopausal osteoporosis, clearly there are also other clinical benefits, such as neuroprotection and lipid/cholesterol reduction [103, 104]. The results of this study reveal that strong PDI inhibition by BAZ can elicit strong neuroprotection both *in vitro* and *in vivo*. Additionally, since PDI is a key component of a protein machinery for lipid packaging and release [105, 106], its inhibition may help explain the lipid/cholesterol-lowering functions of BAZ. Therefore, the present work provides the basis for future explorations of the broader clinical applications of BAZ as an effective PDI inhibitor for different therapeutic benefits.

## Supplementary Information

The online version contains supplementary material available at https://doi.org/10.1186/s12964-025-02209-9.

Supplementary Material 1

Supplementary Material 2

### Authors' contributions

B.T.Z. developed the concept and ideas of this study; obtained financial support; and was responsible for final completion of the manuscript preparation. X.H., Y. W., M. H., L. L., Y. Y. and T. C. took part in performing the experiments and/or data analysis. X. H. also drafted an early version of the manuscript. P.W. and X. C. contributed to development the ideas of this study; involved in the final completion of the manuscript preparation. All authors read and approved the final version of the manuscript.

**Funding**

This study was supported by research grants from Shenzhen Key Laboratory of Steroid Drug Discovery and Development (No. ZDSYS20190902093417963), Shenzhen Peacock Plan (No. KQTD2016053117035204), the National Natural Science Foundation of China (No. 81630096), Shenzhen Bay Laboratory (No. SZBL2019062801007), the 2022 Stable Funding Support Program for Shenzhen Institutions of High Learning, and the Longgang District Science and Technology Bureau's Key Laboratory Program.

### Data availability

No datasets were generated or analysed during the current study.

## Declarations

### Competing interests

The authors declare no competing interests.

Received: 23 August 2024 Accepted: 17 April 2025

### References

1. Dixon SJ, Lemberg KM, Lamprecht MR, Skouta R, Zaitsev EM, Gleason CE, Patel DN, Bauer AJ, Cantley AM, Yang WS, Morrison B 3rd, Stockwell BR. Ferroptosis: an iron-dependent form of nonapoptotic cell death. Cell. 2012;149:1060–72.
2. Hadian K, Stockwell BR. SnapShot: Ferroptosis. Cell. 2020;181:1188-1188.e1181.
3. Feng H, Stockwell BR. Unsolved mysteries: How does lipid peroxidation cause ferroptosis? PLoS Biol. 2018;16:e2006203.
4. Shimada K, Skouta R, Kaplan A, Yang WS, Hayano M, Dixon SJ, Brown LM, Valenzuela CA, Wolpaw AJ, Stockwell BR. Global survey of cell death mechanisms reveals metabolic regulation of ferroptosis. Nat Chem Biol. 2016;12:497–503.
5. Yang WS, Stockwell BR. Ferroptosis: death by lipid peroxidation. Trends Cell Biol. 2016;26:165–76.
6. Cao JY, Dixon SJ. Mechanisms of ferroptosis. Cell Mol Life Sci. 2016;73:2195–209.
7. Carbone M, Melino G. Lipid metabolism offers anticancer treatment by regulating ferroptosis. Cell Death Differ. 2019;26:2516–9.
8. Cai W, Liu L, Shi X, Liu Y, Wang J, Fang X, Chen Z, Ai D, Zhu Y, Zhang X. Alox15/15-HpETE aggravates myocardial ischemia-reperfusion injury by promoting cardiomyocyte ferroptosis. Circulation. 2023;147:1444–60.
9. Maremonti F, Meyer C, Linkermann A. Mechanisms and models of kidney tubular necrosis and nephron loss. J Am Soc Nephrol. 2022;33:472–86.
10. Gao Y, Zhang H, Wang J, Li F, Li X, Li T, Wang C, Li L, Peng R, Liu L, Cui W, Zhang S, Zhang J. Annexin A5 ameliorates traumatic brain injury-induced neuroinflammation and neuronal ferroptosis by modulating the NF-κB/HMGB1 and Nrf2/HO-1 pathways. Int Immunopharmacol. 2023;114:109619.
11. Yamada N, Karasawa T, Kimura H, Watanabe S, Komada T, Kamata R, Sampilvanjil A, Ito J, Nakagawa K, Kuwata H, Hara S, Mizuta K, Sakuma Y, Sata N, Takahashi M. Ferroptosis driven by radical oxidation of n-6 polyunsaturated fatty acids mediates acetaminophen-induced acute liver failure. Cell Death Dis. 2020;11:144.
12. Shen Y, Jin X, Chen W, Gao C, Bian Q, Fan J, Luan J, Cao Z, Guo Z, Gu Y, Liu H, Ju D, Mei X. Interleukin-22 ameliorated acetaminophen-induced kidney injury by inhibiting mitochondrial dysfunction and inflammatory responses. Appl Microbiol Biotechnol. 2020;104:5889–98.
13. Wang Z, Yao M, Jiang L, Wang L, Yang Y, Wang Q, Qian X, Zhao Y, Qian J. Dexmedetomidine attenuates myocardial ischemia/reperfusion-induced ferroptosis via AMPK/GSK-3β/Nrf2 axis. Biomed Pharmacother. 2022;154:113572.
14. Ye J, Lyu TJ, Li LY, Liu Y, Zhang H, Wang X, Xi X, Liu ZJ, Gao JQ. Ginsenoside Re attenuates myocardial ischemia/reperfusion induced ferroptosis via miR-144-3p/SLC7A11. Phytomedicine. 2023;113:154681.
15. Zhu YY, Zhang Q, Jia YC, Hou MJ, Zhu BT. Protein disulfide isomerase plays a crucial role in mediating chemically-induced, glutathione depletion-associated hepatocyte injury in vitro and in vivo. Cell Commun Signal. 2024;22:431.
16. Jaeschke H, Adelusi OB, Akakpo JY, Nguyen NT, Sanchez-Guerrero G, Umbaugh DS, Ding WX, Ramachandran A. Recommendations for the use of the acetaminophen hepatotoxicity model for mechanistic studies and how to avoid common pitfalls. Acta Pharm Sin B. 2021;11:3740–55.
17. Han Q, Sun L, Xiang K. Research progress of ferroptosis in Alzheimer disease: A review. Medicine (Baltimore). 2023;102: e35142.
18. Ryan SK, Ugalde CL, Rolland AS, Skidmore J, Devos D, Hammond TR. Therapeutic inhibition of ferroptosis in neurodegenerative disease. Trends Pharmacol Sci. 2023;44:674–88.
19. Su Y, Jiao Y, Cai S, Xu Y, Wang Q, Chen X. The molecular mechanism of ferroptosis and its relationship with Parkinson's disease. Brain Res Bull. 2024;213:110991.
20. Mahoney-Sánchez L, Bouchaoui H, Ayton S, Devos D, Duce JA, Devedjian JC. Ferroptosis and its potential role in the physiopathology of Parkinson's Disease. Prog Neurobiol. 2021;196:101890.
21. Feng L, Yin X, Hua Q, Ren T, Ke J. Advancements in understanding the role of ferroptosis in hypoxia-associated brain injury: a narrative review. Transl Pediatr. 2024;13:963–75.
22. Alim I, Caulfield JT, Chen Y, Swarup V, Geschwind DH, Ivanova E, Seravalli J, Ai Y, Sansing LH, Ste Marie EJ, Hondal RJ, Mukherjee S, Cave JW, Sagdullaev BT, Karuppagounder SS, Ratan RR. Selenium drives a transcriptional adaptive program to block ferroptosis and treat stroke. Cell. 2019;177:1262-1279.e1225.

23. Wu JR, Tuo QZ, Lei P. Ferroptosis, a recent defined form of critical cell death in neurological disorders. J Mol Neurosci. 2018;66:197–206.
24. Tuo QZ, Lei P, Jackman KA, Li XL, Xiong H, Li XL, Liuyang ZY, Roisman L, Zhang ST, Ayton S, Wang Q, Crouch PJ, Ganio K, Wang XC, Pei L, Adlard PA, Lu YM, Cappai R, Wang JZ, Liu R, Bush AI. Tau-mediated iron export prevents ferroptotic damage after ischemic stroke. Mol Psychiatry. 2017;22:1520–30.
25. Skouta R, Dixon SJ, Wang J, Dunn DE, Orman M, Shimada K, Rosenberg PA, Lo DC, Weinberg JM, Linkermann A, Stockwell BR. Ferrostatins inhibit oxidative lipid damage and cell death in diverse disease models. J Am Chem Soc. 2014;136:4551–6.
26. Liddell JR, Hilton JBW, Kysenius K, Billings JL, Nikseresht S, McInnes LE, Hare DJ, Paul B, Mercer SW, Belaidi AA, Ayton S, Roberts BR, Beckman JS, McLean CA, White AR, Donnelly PS, Bush AI, Crouch PJ. Microglial ferroptotic stress causes non-cell autonomous neuronal death. Mol Neurodegener. 2024;19:14.
27. Tasanen K, Parkkonen T, Chow LT, Kivirikko KI, Pihlajaniemi T. Characterization of the human gene for a polypeptide that acts both as the beta subunit of prolyl 4-hydroxylase and as protein disulfide isomerase. J Biol Chem. 1988;263:16218–24.
28. Pihlajaniemi T, Helaakoski T, Tasanen K, Myllylä R, Huhtala ML, Koivu J, Kivirikko KI. Molecular cloning of the beta-subunit of human prolyl 4-hydroxylase. This subunit and protein disulphide isomerase are products of the same gene. Embo j. 1987;6:643–9.
29. Freedman RB, Hirst TR, Tuite MF. Protein disulphide isomerase: building bridges in protein folding. Trends Biochem Sci. 1994;19:331–6.
30. Cai H, Wang CC, Tsou CL. Chaperone-like activity of protein disulfide isomerase in the refolding of a protein with no disulfide bonds. J Biol Chem. 1994;269:24550–2.
31. Okada K, Fukui M, Zhu BT. Protein disulfide isomerase mediates glutathione depletion-induced cytotoxicity. Biochem Biophys Res Commun. 2016;477:495–502.
32. Hou MJ, Wang P, Zhu BT. Biochemical mechanism of erastin-induced ferroptotic cell death in neuronal cells. Acta Biochim Biophys Sin (Shanghai). 2023;55:853–65.
33. Hou MJ, Huang X, Zhu BT. Mechanism of RSL3-induced ferroptotic cell death in HT22 cells: crucial role of protein disulfide isomerase. Acta Biochim Biophys Sin (Shanghai). 2024;57:616–32.
34. Wu Y, Zhu BT. Role of protein disulfide isomerase in mediating sulfasalazine-induced ferroptosis in HT22 cells: The PDI-NOS-NO-ROS/lipid-ROS cascade. Arch Biochem Biophys. 2025;768:110366.
35. Cheff DM, Huang C, Scholzen KC, Gencheva R, Ronzetti MH, Cheng Q, Hall MD, Arnér ESJ. The ferroptosis inducing compounds RSL3 and ML162 are not direct inhibitors of GPX4 but of TXNRD1. Redox Biol. 2023;62:102703.
36. Lewiecki EM. Bazedoxifene and bazedoxifene combined with conjugated estrogens for the management of postmenopausal osteoporosis. Expert Opin Investig Drugs. 2007;16:1663–72.
37. Masaki H, Imanishi Y, Naka H, Nagata Y, Kurajoh M, Mori K, Emoto M, Miki T, Inaba M. Bazedoxifene improves renal function and increases renal phosphate excretion in patients with postmenopausal osteoporosis. J Bone Miner Metab. 2020;38:405–11.
38. Tian J, Chen X, Fu S, Zhang R, Pan L, Cao Y, Wu X, Xiao H, Lin HJ, Lo HW, Zhang Y, Lin J. Bazedoxifene is a novel IL-6/GP130 inhibitor for treating triple-negative breast cancer. Breast Cancer Res Treat. 2019;175:553–66.
39. Fu S, Chen X, Lo HW, Lin J. Combined bazedoxifene and paclitaxel treatments inhibit cell viability, cell migration, colony formation, and tumor growth and induce apoptosis in breast cancer. Cancer Lett. 2019;448:11–9.
40. Yadav A, Kumar B, Teknos TN, Kumar P. Bazedoxifene enhances the anti-tumor effects of cisplatin and radiation treatment by blocking IL-6 signaling in head and neck cancer. Oncotarget. 2017;8:66912–24.
41. Wei J, Ma L, Lai YH, Zhang R, Li H, Li C, Lin J. Bazedoxifene as a novel GP130 inhibitor for Colon Cancer therapy. J Exp Clin Cancer Res. 2019;38:63.
42. Tsuji J, Li T, Grinshpun A, Coorens T, Russo D, Anderson L, Rees R, Nardone A, Patterson C, Lennon NJ, Cibulskis C, Leshchiner I, Tayob N, Tolaney SM, Tung N, McDonnell DP, Krop IE, Winer EP, Stewart C, Getz G, Jeselsohn R. Clinical efficacy and whole-exome sequencing of liquid biopsies in a phase IB/II study of bazedoxifene and palbociclib in advanced hormone receptor-positive breast cancer. Clin Cancer Res. 2022;28:5066–78.
43. Arevalo MA, Santos-Galindo M, Lagunas N, Azcoitia I, Garcia-Segura LM. Selective estrogen receptor modulators as brain therapeutic agents. J Mol Endocrinol. 2011;46:R1-9.
44. Baez-Jurado E, Rincón-Benavides MA, Hidalgo-Lanussa O, Guio-Vega G, Ashraf GM, Sahebkar A, Echeverria V, Garcia-Segura LM, Barreto GE. Molecular mechanisms involved in the protective actions of Selective Estrogen Receptor Modulators in brain cells. Front Neuroendocrinol. 2019;52:44–64.
45. Lan YL, Wang X, Zou YJ, Xing JS, Lou JC, Zou S, Ma BB, Ding Y, Zhang B. Bazedoxifene protects cerebral autoregulation after traumatic brain injury and attenuates impairments in blood-brain barrier damage: involvement of anti-inflammatory pathways by blocking MAPK signaling. Inflamm Res. 2019;68:311–23.
46. Abdelhamid R, Luo J, Vandevrede L, Kundu I, Michalsen B, Litosh VA, Schiefer IT, Gherezghiher T, Yao P, Qin Z, Thatcher GR. Benzothiophene selective estrogen receptor modulators provide neuroprotection by a novel GPR30-dependent mechanism. ACS Chem Neurosci. 2011;2:256–68.
47. Hao X, Wang Y, Hou MJ, Liao L, Yang YX, Wang YH, Zhu BT. Raloxifene prevents chemically-induced ferroptotic neuronal death in vitro and in vivo. Mol Neurobiol. 2025;62:3934–55.
48. Xie R, Zhao W, Lowe S, Bentley R, Hu G, Mei H, Jiang X, Sun C, Wu Y, Yueying L. Quercetin alleviates kainic acid-induced seizure by inhibiting the Nrf2-mediated ferroptosis pathway. Free Radic Biol Med. 2022;191:212–26.
49. Shao C, Yuan J, Liu Y, Qin Y, Wang X, Gu J, Chen G, Zhang B, Liu HK, Zhao J, Zhu HL, Qian Y. Epileptic brain fluorescent imaging reveals apigenin can relieve the myeloperoxidase-mediated oxidative stress and inhibit ferroptosis. Proc Natl Acad Sci U S A. 2020;117:10155–64.
50. Yang N, Zhang K, Guan QW, Wang ZJ, Chen KN, Mao XY. D-Penicillamine Reveals the Amelioration of Seizure-Induced Neuronal Injury via Inhibiting Aqp11-Dependent Ferroptosis. Antioxidants (Basel). 2022;11:1602.
51. Song Y, Gao M, Wei B, Huang X, Yang Z, Zou J, Guo Y. Mitochondrial ferritin alleviates ferroptosis in a kainic acid-induced mouse epilepsy model by regulating iron homeostasis: Involvement of nuclear factor erythroid 2-related factor 2. CNS Neurosci Ther. 2024;30:e14663.
52. Chen S, Zhao L, Jin X, Liu Q, Xiao Y, Xu H. Astaxanthin inhibits ferroptosis of hippocampal neurons in kainic acid-induced epileptic mice by activating the Nrf2/GPX4 signaling pathway. CNS Neurosci Ther. 2025;31:e70238.
53. Won JP, Yoon HJ, Lee HG, Seo HG. Biochanin A inhibits excitotoxicity-triggered ferroptosis in hippocampal neurons. Eur J Pharmacol. 2024;985:177104.
54. Wang H, Wang P, Zhu BT. Mechanism of erastin-induced ferroptosis in MDA-MB-231 human breast cancer cells: evidence for a critical role of protein disulfide isomerase. Mol Cell Biol. 2022;42:e0052221.
55. Kolodziejski PJ, Rashid MB, Eissa NT. Intracellular formation of "undisruptable" dimers of inducible nitric oxide synthase. Proc Natl Acad Sci U S A. 2003;100:14263–8.
56. Jafari R, Almqvist H, Axelsson H, Ignatushchenko M, Lundbäck T, Nordlund P, Martinez Molina D. The cellular thermal shift assay for evaluating drug target interactions in cells. Nat Protoc. 2014;9:2100–22.
57. Martinez Molina D, Nordlund P. The cellular thermal shift assay: a novel biophysical assay for in situ drug target engagement and mechanistic biomarker studies. Annu Rev Pharmacol Toxicol. 2016;56:141–61.
58. Hong BX, Soong L. Identification and enzymatic activities of four protein disulfide isomerase (PDI) isoforms of Leishmania amazonensis. Parasitol Res. 2008;102:437–46.
59. Tian G, Xiang S, Noiva R, Lennarz WJ, Schindelin H. The crystal structure of yeast protein disulfide isomerase suggests cooperativity between its active sites. Cell. 2006;124:61–73.
60. Lyles MM, Gilbert HF. Catalysis of the oxidative folding of ribonuclease A by protein disulfide isomerase: dependence of the rate on the composition of the redox buffer. Biochemistry. 1991;30:613–9.
61. Biterova EI, Isupov MN, Keegan RM, Lebedev AA, Sohail AA, Liaqat I, Alanen HI, Ruddock LW. The crystal structure of human microsomal triglyceride transfer protein. Proc Natl Acad Sci U S A. 2019;116:17251–60.

62. Wang C, Li W, Ren J, Fang J, Ke H, Gong W, Feng W, Wang CC. Structural insights into the redox-regulated dynamic conformations of human protein disulfide isomerase. Antioxid Redox Signal. 2013;19:36–45.
63. Hosfield DJ, Weber S, Li N-S, Sauvage M, Joiner CF, Hancock GR, Sullivan EA, Ndukwe E, Han R, Cush S, Lainé M, Mader SC, Greene GL, Fanning SW. Stereospecific lasofoxifene derivatives reveal the interplay between estrogen receptor alpha stability and antagonistic activity in ESR1 mutant breast cancer cells. Elife. 2022;11: e72512.
64. Berman HM, Westbrook J, Feng Z, Gilliland G, Bhat TN, Weissig H, Shindyalov IN, Bourne PE. The Protein Data Bank. Nucleic Acids Res. 2000;28:235–42.
65. Waterhouse A, Bertoni M, Bienert S, Studer G, Tauriello G, Gumienny R, Heer FT, de Beer TAP, Rempfer C, Bordoli L, Lepore R, Schwede T. SWISS-MODEL: homology modelling of protein structures and complexes. Nucleic Acids Res. 2018;46:W296–303.
66. Yang YX, Li P, Zhu BT. Binding of Selected Ligands to Human Protein Disulfide Isomerase and Microsomal Triglyceride Transfer Protein Complex and the Associated Conformational Changes: A Computational Molecular Modelling Study. ChemistryOpen. 2025;14:e202400034.
67. Lu C, Wu C, Ghoreishi D, Chen W, Wang L, Damm W, Ross GA, Dahlgren MK, Russell E, Von Bargen CD, Abel R, Friesner RA, Harder ED. OPLS4: improving force field accuracy on challenging regimes of chemical space. J Chem Theory Comput. 2021;17:4291–300.
68. Friesner RA, Murphy RB, Repasky MP, Frye LL, Greenwood JR, Halgren TA, Sanschagrin PC, Mainz DT. Extra precision glide: Docking and scoring incorporating a model of hydrophobic enclosure for protein-ligand complexes. J Med Chem. 2006;49:6177–96.
69. Wang R, Lai L, Wang S. Further development and validation of empirical scoring functions for structure-based binding affinity prediction. J Comput Aided Mol Des. 2002;16:11–26.
70. Vangone A, Schaarschmidt J, Koukos P, Geng C, Citro N, Trellet ME, Xue LC, Bonvin AMJJ. Large-scale prediction of binding affinity in protein–small ligand complexes: the PRODIGY-LIG web server. Bioinformatics. 2018;35:1585–7.
71. Wang C, Zhang Y. Improving scoring-docking-screening powers of protein-ligand scoring functions using random forest. J Comput Chem. 2017;38:169–77.
72. Jo S, Kim T, Iyer VG, Im W. CHARMM-GUI: a web-based graphical user interface for CHARMM. J Comput Chem. 2008;29:1859–65.
73. Vanommeslaeghe K, Hatcher E, Acharya C, Kundu S, Zhong S, Shim J, Darian E, Guvench O, Lopes P, Vorobyov I, Mackerell AD Jr. CHARMM general force field: A force field for drug-like molecules compatible with the CHARMM all-atom additive biological force fields. J Comput Chem. 2010;31:671–90.
74. Huang J, Rauscher S, Nawrocki G, Ran T, Feig M, de Groot BL, Grubmuller H, MacKerell AD. CHARMM36m: an improved force field for folded and intrinsically disordered proteins. Nature Methods. 2017;14:71–3.
75. Jorgensen WL, Chandrasekhar J, Madura JD, Impey RW, Klein ML. Comparison of simple potential functions for simulating liquid water. J Chem Phys. 1983;79:926–35.
76. Beglov D, Roux B. Finite representation of an infinite bulk system - solvent boundary potential for computer-simulations. J Chem Phys. 1994;100:9050–63.
77. Phillips JC, Braun R, Wang W, Gumbart J, Tajkhorshid E, Villa E, Chipot C, Skeel RD, Kale L, Schulten K. Scalable molecular dynamics with NAMD. J Comput Chem. 2005;26:1781–802.
78. Izaguirre JA, Catarello DP, Wozniak JM, Skeel RD. Langevin stabilization of molecular dynamics. J Chem Phys. 2001;114:2090–8.
79. Darden T, York D, Pedersen L. Particle Mesh Ewald - an N.Log(N) method for ewald sums in large systems. J Chem Phys. 1993;98:10089–92.
80. Essmann U, Perera L, Berkowitz ML, Darden T, Lee H, Pedersen LG. A Smooth Particle Mesh Ewald Method. J Chem Phys. 1995;103:8577–93.
81. Feller SE, Zhang YH, Pastor RW, Brooks BR. Constant-pressure molecular-dynamics simulation - the langevin piston method. J Chem Phys. 1995;103:4613–21.
82. Choi HJ, Lee AJ, Kang KS, Song JH, Zhu BT. 4-Hydroxyestrone, an endogenous estrogen metabolite, can strongly protect neuronal cells against oxidative damage. Sci Rep. 2020;10:7283.
83. Carroll JC, Rosario ER, Chang L, Stanczyk FZ, Oddo S, LaFerla FM, Pike CJ. Progesterone and estrogen regulate Alzheimer-like neuropathology in female 3xTg-AD mice. J Neurosci. 2007;27:13357–65.
84. Lee GY, Lee C, Park GH, Jang JH. Amelioration of scopolamine-induced learning and memory impairment by α-pinene in C57BL/6 Mice. Evid Based Complement Alternat Med. 2017;2017:4926815.
85. Zhang Y, Kurup P, Xu J, Carty N, Fernandez SM, Nygaard HB, Pittenger C, Greengard P, Strittmatter SM, Nairn AC, Lombroso PJ. Genetic reduction of striatal-enriched tyrosine phosphatase (STEP) reverses cognitive and cellular deficits in an Alzheimer's disease mouse model. Proc Natl Acad Sci U S A. 2010;107:19014–9.
86. Ramdial K, Franco MC, Estevez AG. Cellular mechanisms of peroxynitrite-induced neuronal death. Brain Res Bull. 2017;133:4–11.
87. Song X, Hao X, Zhu BT. Role of mitochondrial reactive oxygen species in chemically-induced ferroptosis. Free Radic Biol Med. 2024;223:473–92.
88. Ohno M, Sametsky EA, Younkin LH, Oakley H, Younkin SG, Citron M, Vassar R, Disterhoft JF. BACE1 deficiency rescues memory deficits and cholinergic dysfunction in a mouse model of Alzheimer's disease. Neuron. 2004;41:27–33.
89. Damjanac M, Rioux Bilan A, Barrier L, Pontcharraud R, Anne C, Hugon J, Page G. Fluoro-Jade B staining as useful tool to identify activated microglia and astrocytes in a mouse transgenic model of Alzheimer's disease. Brain Res. 2007;1128:40–9.
90. Shan XM, Lu C, Chen CW, Wang CT, Liu TT, An T, Zhu ZY, Zou DW, Gao YB. Tangshenning formula alleviates tubular injury in diabetic kidney disease via the Sestrin2/AMPK/PGC-1α axis: Restoration of mitochondrial function and inhibition of ferroptosis. J Ethnopharmacol. 2025;345: 119579.
91. Nakamura Y, Yamamoto T, Kobayashi S, Suetomi T, Uchinoumi H, Oda T, Sano M, Yano M. Concomitant administration of dantrolene is sufficient to protect against doxorubicin-induced cardiomyopathy. JACC CardioOncol. 2025;7:38–52.
92. Yan J, Li Z, Liang Y, Yang C, Ou W, Mo H, Tang M, Chen D, Zhong C, Que D, Feng L, Xiao H, Song X, Yang P. Fucoxanthin alleviated myocardial ischemia and reperfusion injury through inhibition of ferroptosis via the NRF2 signaling pathway. Food Funct. 2023;14:10052–68.
93. Niu C, Jiang D, Guo Y, Wang Z, Sun Q, Wang X, Ling W, An X, Ji C, Li S, Zhao H, Kang B. Spermidine suppresses oxidative stress and ferroptosis by Nrf2/HO-1/GPX4 and Akt/FHC/ACSL4 pathway to alleviate ovarian damage. Life Sci. 2023;332:122109.
94. Liu B, Wang H. Oxaliplatin induces ferroptosis and oxidative stress in HT29 colorectal cancer cells by inhibiting the Nrf2 signaling pathway. Exp Ther Med. 2022;23:394.
95. Luo Y, Zhang Y, Pang S, Min J, Wang T, Wu D, Lin C, Xiao Z, Xiang Q, Li Q, Ma L. PCBP1 protects bladder cancer cells from mitochondria injury and ferroptosis by inducing LACTB mRNA degradation. Mol Carcinog. 2023;62:907–19.
96. Hoffstrom BG, Kaplan A, Letso R, Schmid RS, Turmel GJ, Lo DC, Stockwell BR. Inhibitors of protein disulfide isomerase suppress apoptosis induced by misfolded proteins. Nat Chem Biol. 2010;6:900–6.
97. Sun X, Hao X, Jia YC, Zhang Q, Zhu YY, Yang YX, Zhu BT. Protective effect of 2-hydroxyestrone and 2-hydroxyestradiol against chemically induced hepatotoxicity in vitro and in vivo. J Pharmacol Exp Ther. 2025;392:100050.
98. Huang X, Hou MJ, Zhu BT. Protection of HT22 neuronal cells against chemically-induced ferroptosis by catechol estrogens: protein disulfide isomerase as a mechanistic target. Sci Rep. 2024;14:23988.
99. Zhang Q, Hao X, Sun X, Jia YC, Zhu YY, Yang YX, Zhu BT. 4-Hydroxyestrogen metabolites strongly prevent chemically-induced ferroptotic hepatocyte injury in vitro and in vivo. Eur J Pharmacol. 2025;993:177313.
100. Yang YX, Li P, Wang P, Zhu BT. 17β-Estradiol-Induced Conformational Changes of Human Microsomal Triglyceride Transfer Protein: A Computational Molecular Modelling Study. Cells. 2021;10:1566.
101. Yang WS, SriRamaratnam R, Welsch ME, Shimada K, Skouta R, Viswanathan VS, Cheah JH, Clemons PA, Shamji AF, Clish CB, Brown LM, Girotti AW, Cornish VW, Schreiber SL, Stockwell BR. Regulation of ferroptotic cancer cell death by GPX4. Cell. 2014;156:317–31.
102. Conlon M, Poltorack CD, Forcina GC, Armenta DA, Mallais M, Perez MA, Wells A, Kahanu A, Magtanong L, Watts JL, Pratt DA, Dixon SJ. A compendium of kinetic modulatory profiles identifies ferroptosis regulators. Nat Chem Biol. 2021;17:665–74.

103. Komm BS, Kharode YP, Bodine PV, Harris HA, Miller CP, Lyttle CR. Bazedoxifene acetate: a selective estrogen receptor modulator with improved selectivity. Endocrinology. 2005;146:3999–4008.
104. Duggan ST, McKeage K. Bazedoxifene: a review of its use in the treatment of postmenopausal osteoporosis. Drugs. 2011;71:2193–212.
105. Sirtori CR, Pavanello C, Bertolini S. Microsomal transfer protein (MTP) inhibition-a novel approach to the treatment of homozygous hypercholesterolemia. Ann Med. 2014;46:464–74.
106. Berberich AJ, Hegele RA. Lomitapide for the treatment of hypercholesterolemia. Expert Opin Pharmacother. 2017;18:1261–8.

## Publisher's Note